

Tunable ferroelectricity in oxygen-deficient perovskites

Yongjin Shin¹ and Giulia Galli^{1,2,3,*}

¹*Pritzker School of Molecular Engineering, University of Chicago, Chicago, Illinois 60637, United States*

²*Department of Chemistry, University of Chicago, Chicago, Illinois 60637, United States*

³*Center for Molecular Engineering and Materials Science Division, Argonne National Laboratory, Lemont, Illinois 60439, United States*

Using first-principles calculations, we predict that tunable ferroelectricity can be realized in oxide perovskites with the Grenier structure and ordered oxygen vacancies. Specifically, we show that $R_{1/3}A_{2/3}\text{FeO}_{2.67}$ solids (where R is a rare-earth ion and A an alkaline-earth cation) exhibit stable polar phases, with a spontaneous polarization tunable by an appropriate choice of R and A . We find that larger cations combined with small R elements lead to a maximum in the polarization and to a minimum in the energy barriers required to switch the sign of the polarization. Ferroelectricity arises from cooperative distortions of octahedral and tetrahedral units, where a combination of rotational and sliding modes controls the emergence of polarization within three-dimensional connected layers. Our results indicate that polar Grenier phases of oxide perovskites are promising materials for microelectronic applications and, in general, for the study of phenomena emerging from breaking inversion symmetry in solids.

I. INTRODUCTION

Ferroelectric materials have found many interesting applications in electronic and memory devices, and understanding and engineering their properties is a topic of great interest in condensed matter physics and materials science [1–6]. Ferroelectricity can be realized in polar solids without inversion symmetry, for example by relying on second-order Jahn-Teller distortions occurring in systems composed of elements with d^0 electronic configurations [7], or on the presence of *lone pair* ns^2 configurations e.g., in heavy elements [2].

Oxides represent an interesting class of materials where ferroelectricity has been realized. While there are only few transition metal oxides with partially filled d -orbitals [8, 9], some layered oxide perovskites structures exhibit a ferroelectric behavior due to the geometric arrangements of layers [10–13]. An emerging route to stabilize a polar phase in oxides is the utilization of symmetry breaking in oxygen-deficient perovskites ($ABO_{3-\delta}$), for example brownmillerites where oxygen vacancies are perfectly ordered [14–17].

In oxides with the ABO_3 perovskite structure shown in Fig. 1, oxygen vacancies with long-range order are formed along specific crystallographic directions, leading to the transformation of BO_6 octahedral units into BO_4 tetrahedral chains. Depending on how these chains are ‘twisted’ (see Fig. 2) polar structures may be formed; however, in many instances such structures [18–21] are metastable or only marginally stable [18, 22–24], thus limiting their use in devices.

One promising oxygen-deficient perovskite is the so-called Grenier phase, whose oxygen deficiency ($\delta = 1/3$) is smaller than that of brownmillerites ($\delta = 0.5$) [25–27]. Grenier and brownmillerite phases differ by the stacking and periodicity of tetrahedral chains (Fig. 1) formed by oxygen vacancies. While brownmillerite solids have been extensively investigated for a variety of applications, e.g. as possible constituents of neuromorphic de-

vices or as ionic conductors [28–32], Grenier phases are much less studied [33–40]. However, recent experiments observed a spontaneous polarization coexisting with antiferromagnetism in $R_{1.2}\text{Ba}_{1.2}\text{Ca}_{0.6}\text{Fe}_3\text{O}_8$ ($R = \text{Gd}, \text{Tb}$) [41], pointing at the possibility of realizing stable polar Grenier phases and hence interesting ferroelectric materials, which could be used, for example, as neuromorphic devices [9, 42].

In this work, using first principles calculations we predict that tunable ferroelectricity can be realized in oxygen-deficient $R_{1/3}A_{2/3}\text{FeO}_{2.67}$ ($=RA_2\text{Fe}_3\text{O}_8$) perovskites with ordered oxygen vacancies. In particular we show that polar Grenier and antipolar brownmillerite phases may be realized, with the polarization determined by cooperative distortions that can be tuned by the choice of the cations. Specifically, larger A alkali-earth cations, e.g., Ba and smaller R rare-earth elements, e.g. Tb, lead to a maxi-

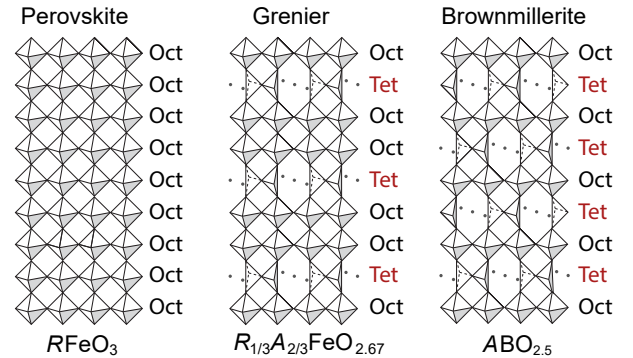


FIG. 1. **Structures of oxygen-deficient perovskites.** Schematic illustration of the $R\text{FeO}_3$ perovskite (left), $R_{1/3}A_{2/3}\text{FeO}_{2.67}$ Grenier (middle), and $A\text{FeO}_{2.5}$ brownmillerite structure (right). R -ions and A -cations are omitted for clarity, and vacancy sites are drawn as gray dots. Note that the stacking sequence of the Grenier phase is OOTO..., with two octahedral (O) layers sandwiched between tetrahedral (T) layers, and that of the brownmillerite phase is OTOTOT....

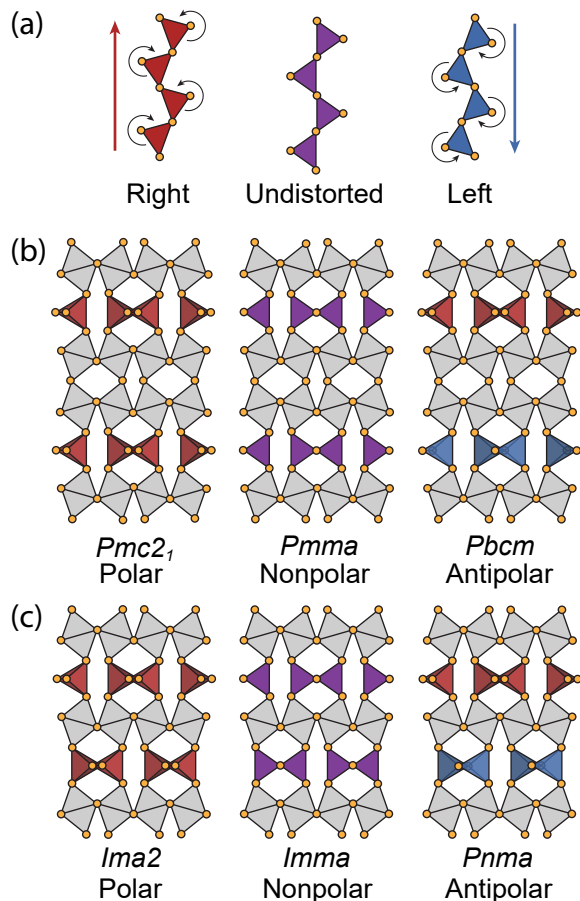


FIG. 2. Arrangements of tetrahedral chains and corresponding distortion patterns in oxygen-deficient phases. Twisting of tetrahedral chains (a) in oxygen-deficient perovskites with ordered oxygen vacancies. Symmetry breaking in (b) brownmillerite and (c) Grenier phases due to the twisting of tetrahedral chains. We omitted A -cations and R -ions for clarity, and oxygen atoms are depicted as yellow circles. Note the difference in space group, given below each structure, depending on the twisting of the chains. In high symmetry, nonpolar phases, the chains are in undistorted positions. In polar phases, all tetrahedral chains are aligned, while in antipolar phases two nearest tetrahedral layers exhibit opposite chain twisting. Other distortion patterns induced by chain twisting and observed in large unit cells are discussed in the Supplementary Information (SI).

imum in the spontaneous polarization of the solid and to a minimum in the energy barriers required to induce a switch in the sign of the polarization.

II. RESULTS

Using first principles calculations based on Density Functional Theory (DFT), we investigated the properties of $R_{1/3}A_{2/3}FeO_{2.67}$ solids as a function of the rare-earth element R and cation A . We considered $A = Ca, Sr,$ and Ba and lanthanides from La to Tm , which are known to

TABLE I. Energy differences (ΔE , meV/f.u.) referred to the ground state energies for prototypical oxygen-deficient perovskites.

System	$Nd_{1/3}Ca_{2/3}FeO_{2.67}$	$CaFeO_{2.5}$
Structure type	Grenier	Brownmillerite
ΔE (neutral)	263.1	330.1
ΔE (polar)	0	22.24
ΔE (antipolar)	38.01	0

form $RFeO_3$ perovskite structures [43–50]. We excluded Yb and Lu from our study as those elements were found to lead to metallic Grenier structures.

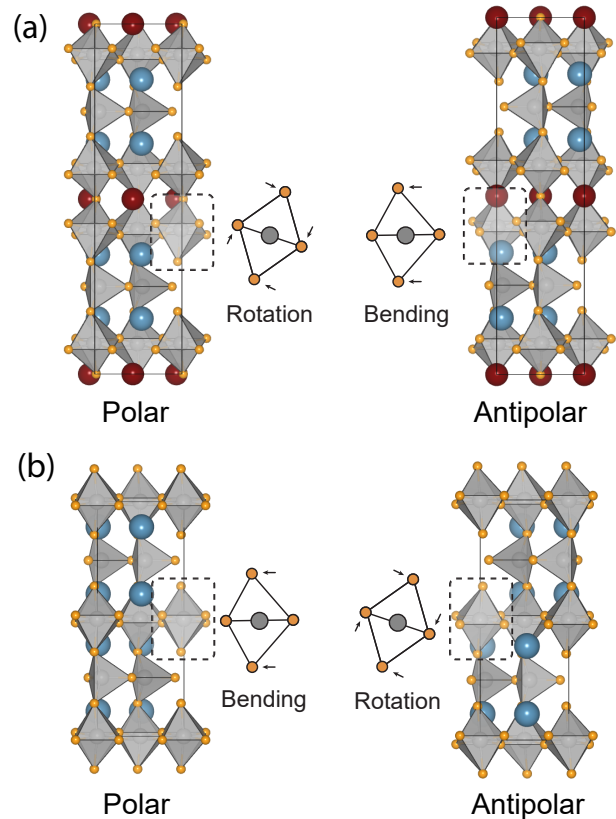


FIG. 3. Distortion patterns in polar and antipolar phases. Octahedral distortions in polar and antipolar phases of (a) Grenier ($R_{1/3}A_{2/3}FeO_{2.67}$) and (b) brownmillerite ($AFeO_{2.5}$) structures. Red and blue spheres indicate R -ions and A -cations, respectively. Oxygen atoms are represented as yellow circles.

A. Ferroelectricity from cooperative distortions

We start by considering $Nd_{1/3}Ca_{2/3}FeO_{2.67}$ and $CaFeO_{2.5}$ as representative compounds with the Grenier and brownmillerite structure, respectively, because these materials have been investigated in several experiments

[22, 34, 38, 40]. In these systems, the oxidation state of Fe is 3+; Fe has a high-spin d^5 electronic configuration, leading to antiferromagnetic (AFM) Fe-Fe coupling, based on Goodenough-Kanamori-Anderson (GKA) superexchange rules [51–53]. Hence in our calculations we constrained $\text{Nd}_{1/3}\text{Ca}_{2/3}\text{FeO}_{2.67}$ and $\text{CaFeO}_{2.5}$ to have G-type AFM order in all brownmillerite and Grenier phases, consistent with the findings of previous studies [19, 40, 41, 54, 55]. (See SI for details on magnetic ordering).

In Fig. 2 we show how different twisting of tetrahedral chains leads to polar, nonpolar or antipolar structures [18–20, 27]. Our total energy calculations for $\text{Nd}_{1/3}\text{Ca}_{2/3}\text{FeO}_{2.67}$ and $\text{CaFeO}_{2.5}$ show that polar structures can only be stabilized for Grenier phases, while antipolar structures can only be stabilized in brownmillerite phases (see Table I). These results point at the key role of oxygen vacancy concentration (δ) in oxygen-deficient perovskites ($\text{ABO}_{3-\delta}$) to obtain the desired ferroelectric behavior, specifically, a δ value of $1/3$ is required to realize polar phases.

Interestingly, we find that cooperative distortions are responsible for the stabilization of a polar (antipolar) phase in Grenier (brownmillerite) structures. In particular, as shown in Fig. 3, rotations (bending) of octahedral units lead to antipolar (polar) structures in brownmillerite, while the opposite happens in Grenier phases, where rotations (bending) of the units lead to polar (antipolar) structures.

One may intuitively understand the emergence of ferroelectricity in Grenier phases by drawing an analogy between cooperative distortions and gear motion, as shown in Fig. 4. Upon rotation of octahedral and twisting of tetrahedral units, the apical oxygen atoms of the octahedral units move in opposite directions, whereas the ones in the tetrahedral units move in the same direction [Fig. 4(a,b)]. We may then view octahedral layers as rotating gears, and tetrahedral layers as sliding gears. Hence ferroelectricity arises from the combination of the rotational and sliding motion of octahedra and tetrahedra, respectively. We note that these cooperative distortions occur without any off-center displacement of Fe atoms, consistent with the general trend observed for systems with partially filled d -orbitals [8].

Having identified which structural motifs lead to polar phases, we calculated the spontaneous polarization of the solids using DFT+ U and the Berry-phase method [56, 57]. For $\text{Nd}_{1/3}\text{Ca}_{2/3}\text{FeO}_{2.67}$ we obtained $2.24 \mu\text{C}/\text{cm}^2$, a value which is insensitive to the choice of the U value, with variations within $0.11 \mu\text{C}/\text{cm}^2$ when U is varied between 4 to 7 eV. (SI). This value is smaller than that reported experimentally [41] for $R_{1.2}\text{Ba}_{1.2}\text{Ca}_{0.6}\text{Fe}_3\text{O}_8$ ($R = \text{Tb}, \text{Gd}$), most likely due to the difference of R and A cations, as discussed in the next section. In Fig. 5(b), we show the difference in polarization between the nonpolar and the polar phases. Assuming that the path identified here is indeed the lowest energy path, we find that the energy barrier to switch the sign of the polarization is 263 meV/f.u. for $\text{Nd}_{1/3}\text{Ca}_{2/3}\text{FeO}_{2.67}$. This barrier is larger than that found in $\text{SrFeO}_{2.5} \sim 150$ meV/f.u. [23]),

possibly because of smaller R -ions and A -cations.

In order to better understand the mechanism leading to ferroelectricity, it is useful to analyze the contributions of each layer to the total polarization. To this end, we plot the layer polarization along the polar (z) direction in Fig. 5(a), computed by summing, for each constituent ion (n), the products of Born effective charges (Z^*) and the displacement of ions from the centro-symmetric site (Δu) along the polar direction:

$$P_z = \frac{e}{\Omega} \sum_n Z_{zz,n}^* \Delta u_{z,n}, \quad (1)$$

Here e is the electron charge and Ω is the volume of the unit cell. As shown in Fig. 5(a), the tetrahedral chains give rise to local dipole moments, with additional, significant contributions of opposite sign from CaO layers (negative contribution) and NdO layers (positive contribution).

We note that our results are qualitatively different from those of the model suggested in Ref. 41, which predicts positive contributions to the polarization from all atomic layers and contributions from RO and AO layers smaller than those found here. In the model of Ref. 41 all apical oxygen atoms are displaced in the same direction.

The ferroelectricity found here in $\text{Nd}_{1/3}\text{Ca}_{2/3}\text{FeO}_{2.67}$ Grenier phases originates from the presence of *two* octahedral layers between pairs of tetrahedral layers, i.e. the emergence of ferroelectricity is critically dependent not only on oxygen deficiency but also on the stacking of layers, which differs from the stacking found in brownmillerite composed only of *one* octahedral layer between pairs of tetrahedral ones. Our results also indicate that any even number of intercalated octahedral layers would lead to the stabilization of a polar phase. However, to the best of our knowledge, there is no compound with a number of intercalated octahedral layers larger than two (as in Grenier structures); hence we consider Grenier structures as the optimal solution for designing ferroelectricity in the class of materials studied here, and in the next section we consider only solids with the Grenier stacking.

B. Cation size-effect in ferroelectricity

We now turn to discuss the effect of the size of R -ions and A -cations in determining the ferroelectric properties of $R_{1/3}A_{2/3}\text{FeO}_{2.67}$. In Fig. 2 we consider a cation ordering in which the R -ions are located between the octahedral layers because our total energy calculations as a function of cation orderings in $\text{Nd}_{1/3}\text{Ca}_{2/3}\text{FeO}_{2.67}$ showed that the rare earth preferably occupies the A -site in octahedral units (see SI). The ordering chosen here is also consistent with the cation occupancies reported in the literature for $\text{La}_{1/3}\text{Sr}_{2/3}\text{FeO}_{2.67}$ and $\text{Nd}_{1/3}\text{Ca}_{2/3}\text{FeO}_{2.67}$ [40].

In Fig. 6, we show the total energy difference between polar and nonpolar phases as a function of R and A . For all $R_{1/3}A_{2/3}\text{FeO}_{2.67}$ systems we find that the polar phase is more stable than the antipolar one and small-size R and A contribute to the stabilization of the polar phase.

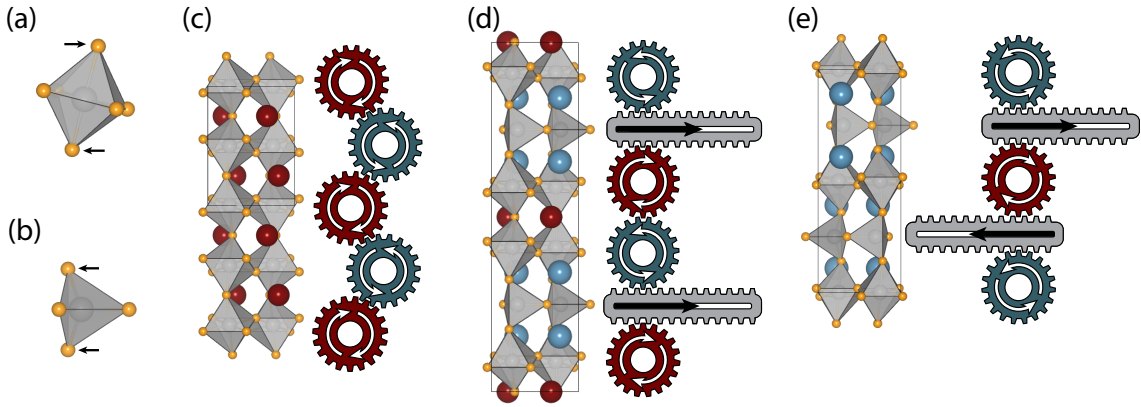


FIG. 4. **Cooperative distortions and gear motions.** Cooperative distortions of polyhedral units in perovskite, brownmillerite, and Grenier phase: (a) Rotation of octahedra and (b) twisting of tetrahedral chains. Stable distortion patterns in (c) $R\text{FeO}_3$ perovskite, (d) $R_{1/3}A_{2/3}\text{FeO}_{2.67}$, and (e) $A\text{FeO}_{2.5}$, where octahedral and tetrahedral layers are shown as rotational and sliding gears, respectively. For brownmillerite, there is a single rotational gear (octahedral layer) between sliding gears (tetrahedral layers) and the two nearest sliding gears move in opposite direction. In Grenier phases, the additional rotational gear (arising from the different octahedral layer stacking) leads to an opposite rotation, and the sliding gears move in the same direction.

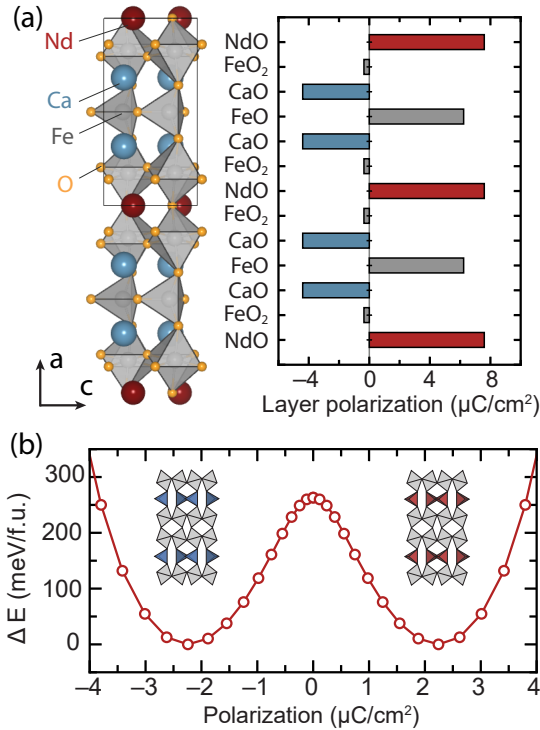


FIG. 5. **Polarization and switching barrier in $\text{Nd}_{1/3}\text{Ca}_{2/3}\text{FeO}_{2.67}$.** (a) Layer-by-layer projection of the polarization in the $\text{Nd}_{1/3}\text{Ca}_{2/3}\text{FeO}_{2.67}$ Grenier phase (see text). (b) Total energy difference between two polar phases with opposite polarizations as a function of the polarization.

The systems with the smallest cations ($R = \text{Tm}$, $A = \text{Ca}$) exhibit the largest energy differences between different phases, and the polar phase is 123 and 320 meV/f.u. lower than antipolar and nonpolar phases, respectively. On the

other hand, for larger cations (e.g. $R = \text{La}$, $A = \text{Ba}$) we find that these energy differences almost vanish (they are less than 1 meV/f.u.), indicating that in the Grenier structure all phases are nearly degenerate.

Interestingly, we find that for all R -ions, only the polar phase can be stabilized. In Fig. 6, we show that the energy difference between antipolar and nonpolar phases is not sensitive to the size of the R -ion, since the local geometries surrounding the element R are similar in the nonpolar and antipolar phases, whose main difference is the twisting of the tetrahedral chains. For example in systems with $A = \text{Ca}$ shown in Fig. 6(a), the energy difference between nonpolar and antipolar phases shows a weak variation from 197 meV/f.u. for $R = \text{Tm}$ to 224 meV/f.u. for $R = \text{La}$. On the other hand, the energy differences between nonpolar, polar, and antipolar phases vary substantially as a function of the A cation. The energy difference decreases by 50% when going from from Ca to Sr , and is again halved in the case of Ba .

Based on our results on total energy differences and the layer-by-layer projection of the polarization presented in Fig. 5(a), we identify three major geometrical descriptors for the emergence of the polarization in Fig. 7(a,b): the twist angle of tetrahedral chains (θ_{twist}) and the displacements of $R - \text{O}$ pairs along the polar direction ($\Delta u_{z,R-\text{O}}$) and of $A - \text{O}$ pairs ($\Delta u_{z,A-\text{O}}$). We found that these geometrical parameters undergo substantial variations, depending on the choice of R and A (see SI). For example, for $\text{Nd}_{1/3}\text{Ca}_{2/3}\text{FeO}_{2.67}$ (small cation), $\Delta u_{z,R-\text{O}} = 0.45 \text{ \AA}$ and $\Delta u_{z,A-\text{O}} = 0.47 \text{ \AA}$, while for $\text{La}_{1/3}\text{Sr}_{2/3}\text{FeO}_{2.67}$ (large cation), those values are smaller, 0.14 and 0.19 \AA , respectively, as shown in Fig. 7(b). On the other hand, the difference in θ_{twist} is relatively small, with the angle of $\text{Nd}_{1/3}\text{Ca}_{2/3}\text{FeO}_{2.67}$ being 51.5° and that of $\text{La}_{1/3}\text{Sr}_{2/3}\text{FeO}_{2.67}$ 48.7° .

In Fig. 7(b), we show the polarization as a function of

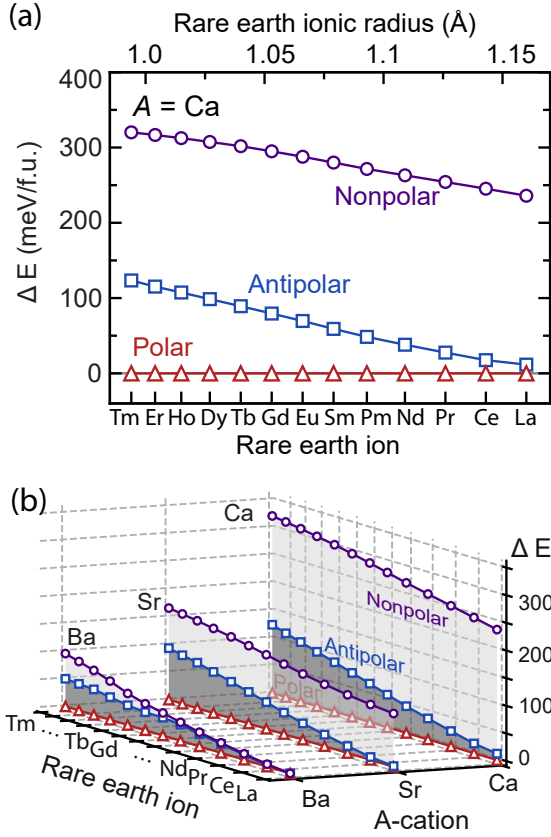


FIG. 6. Cation-dependent energy differences between distortion patterns in Grenier structure. (a) Energy difference between nonpolar, antipolar and polar phases in Grenier structures of $R_{1/3}A_{2/3}\text{FeO}_{2.67}$ as a function of R -ions. (b) Total energy difference between nonpolar, antipolar, and polar phases as a function of A -cation and R -ions. Two-dimensional projections for $A = \text{Sr}$ and Ba are provided in SI.

R and A , exhibiting a maximum for $R = \text{Tm}$ and $A = \text{Ba}$. This cation selection gives rise to the largest $\Delta u_{z,R-O}$ and smallest $\Delta u_{z,A-O}$, which in turn maximize the spontaneous polarization. We note that the value found here for the polarization is lower than the values reported experimentally, ranging from 23.2 to 33.0 $\mu\text{C}/\text{cm}^2$ [41]. Different reasons may be responsible for this discrepancy. From a theoretical standpoint, the absolute value of P is expected to depend on the choice of the functionals [58], and the trend shown in Fig. 7, more than the absolute values, should be considered to define a reliable roadmap for ferroelectric design. It is noteworthy though that the polarization values computed here are not sensitive to the choice of the U value (see SI). We also note that the chemical formula of $R_{1.2}\text{Ba}_{1.2}\text{Ca}_{0.6}\text{Fe}_3\text{O}_8$ ($R = \text{Gd}, \text{Tb}$) reported experimentally deviates from that of the stoichiometric $R_{1/3}A_{2/3}\text{FeO}_{2.67}$ considered here, and may involve cation disorder. We conclude that smaller R such as Tm and larger A such as Ba are optimal choices for enhancing ferroelectricity of polar Grenier structures. In addition, given that the primary switching barrier is formed be-

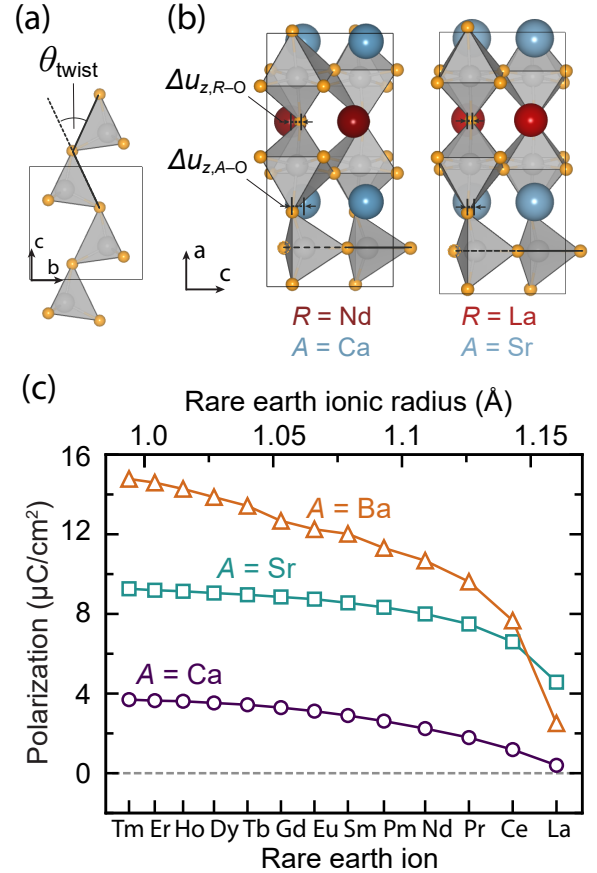


FIG. 7. Geometric descriptors of the polar $R_{1/3}A_{2/3}\text{FeO}_{2.67}$ phases and the effect of cation size in polarization. (a) Twist angle (θ_{twist}) of tetrahedral chains in polar Grenier phase of $\text{Nd}_{1/3}\text{Ca}_{2/3}\text{FeO}_{2.67}$. (b) Atomic structure and polar displacements in RO and AO layers in polar Grenier phases of $\text{Nd}_{1/3}\text{Ca}_{2/3}\text{FeO}_{2.67}$ and $\text{La}_{1/3}\text{Sr}_{2/3}\text{FeO}_{2.67}$. (c) Spontaneous polarization of $R_{1/3}A_{2/3}\text{FeO}_{2.67}$ as a function of the rare-earth ion.

tween the polar and nonpolar phases, we find that small A -cations, e.g. Ca, lead to a high energy barrier. While our results show that the energy barrier also changes depending on the choice of R , the polarization value does not substantially vary when R is smaller than Gd [Fig. 7(b)]. Specifically, changing R from the smallest member (Tm) of the set to the slightly larger Tb in $R_{1/3}\text{Ba}_{2/3}\text{FeO}_{2.67}$ would decrease the spontaneous polarization from 14.8 to 13.4 $\mu\text{C}/\text{cm}^2$. For $A = \text{Sr}$ and Ca , the decrease in polarization is 0.30 and 0.26 $\mu\text{C}/\text{cm}^2$, respectively. This small variation of P indicates that several R elements such as Tb, Dy, and Ho may be chosen to obtain a similar ferroelectric behaviour in Grenier structures.

III. DISCUSSION

Using the results of first-principles calculations we proposed that Grenier structures arising from oxygen-vacancy ordering in 3D oxide perovskites are interesting materials to realize ferroelectricity. In Grenier structures polar phases are stabilized by the cooperative motion of octahedral and tetrahedral units, with the twisting motion of tetrahedral chains playing a key role in forming local dipole moments. We considered in particular $R_{1/3}A_{2/3}\text{FeO}_{2.67}$ solids, where the oxidation state of Fe is +3, and whose composition is optimal to grow Grenier rather than brownmillerite structures [59]. We investigated the emergence of ferroelectricity in $R_{1/3}A_{2/3}\text{FeO}_{2.67}$ as a function of the size of the rare-earth and alkali-earth elements, and provided a strategy to choose optimal elements to obtain polar phases. Interestingly, Grenier structures can also be present in superlattices. For example in Ref. 60, the introduction of oxygen vacancies in $(\text{LaFeO}_3)_2/(\text{SrFeO}_3)$ superlattices was shown to form polar domains. Despite a different ratio of La to Sr compared to the ratios considered here, it is reasonable to expect that Grenier phases formed at interfaces may be responsible for the polar domains observed in the films.

We emphasize that the mechanism leading to ferroelectricity in Grenier phases, which exhibits three-dimensional connectivities of polyhedra, is distinct from that responsible for the same phenomenon in other perovskite materials. For example, in the layered Ruddlesden-Popper and Dion-Jacobson phases [12, 61], octahedra are connected in only two dimensions, and a hybrid improper mechanism is responsible [12, 13, 62] for ferroelectricity, where two nonpolar rotational modes of octahedral units give rise to a finite polarization. Other materials with Ruddlesden-Popper phases, for example hybrid organic-inorganic halide perovskites [63] exhibit ferroelectricity arising from the anisotropic shape of organic molecules, which leads to distortions of the octahedral units. The ferroelectricity of Grenier phases also differs from that of oxygen-deficient oxides with defect-like vacancies, e.g. in $\text{SrMnO}_{3-\delta}$ and $\text{SmFeO}_{3-\delta}$ [64, 65].

Overall, our work suggests that Grenier phases can be a rich platform for novel materials phenomena arising from breaking inversion symmetry in solids. The geometrically driven ferroelectric behavior observed in Grenier phases can be extended to other d -electron configurations by adjusting the R/A ratio or incorporating different transition metals. Notably, oxides containing elements such as Mn, Al, Ga, and In, which are known to be compatible with tetrahedral coordination, can form Grenier or brownmillerite structures [21, 33, 66, 67]. By exploring the chemistry of polar Grenier phases, we anticipate exciting opportunities to realize materials with multiferroic properties and investigate optical coupling with ferroelectricity. This line of inquiry could pave the way for utilizing Grenier phases in energy-efficient computing devices, where the inherent hysteresis of ferroelectricity can help realize nonvolatile memories for neuromorphic devices [9, 42].

IV. METHODS

We performed density function theory (DFT) calculations with the generalized gradient corrected functional proposed by Perdew-Burke-Ernzerhof (PBE) [68], and using the plane wave code Quantum ESPRESSO (QE) [69–71], with a U parameter [72] for Fe of 6.5 eV. This U value was determined by matching the experimental band gap of the $\text{SrFeO}_{2.5}$ brownmillerites [73]. We find the calculated total energies and polarization values are relatively insensitive to the choice of U (see SI). We used projected augmented wave (PAW) pseudopotentials from the PSLibrary [74], except for La where we used the Rare Earth PAW datasets [75]. For rare-earth elements, f -electrons were considered as part of the core and we used pseudopotentials having 11 valence electrons, assuming a 3+ charge state of each element. We used a kinetic energy cutoff of 75 Ry for wavefunctions and 300 Ry for the charge density. The Brillouin zone was sampled with a $3 \times 8 \times 8$ k -grid for Grenier structures whose unit cell size is $6a_{\text{pc}} \times 2\sqrt{2}a_{\text{pc}} \times 2\sqrt{2}a_{\text{pc}}$, where a_{pc} denotes the pseudocubic lattice parameter of perovskites. The cell parameters and atomic coordinates were optimized with a threshold of 3×10^{-4} Ry/Bohr (~ 0.01 eV/Å) on the atomic forces. We carried out calculations for $R_{1/3}A_{2/3}\text{FeO}_{2.67}$ solids with different choices of R and A elements: R is a lanthanide elements from La to Tm, where $R\text{FeO}_3$ solids are known to form perovskite structures [43–50]; $A = \text{Ca}, \text{Sr}, \text{and Ba}$. When comparing the size of rare-earth cations, we used 8-coordinate ionic radii [76], similar to nickelate perovskite studies [77, 78]. Although the R cations are expected to be 12-fold coordinated in cubic perovskites, the nickelates possess GdFeO_3 -type distortions, which reduce the R cation coordination. Visualization of atomic structures was done with the VESTA package [79].

ACKNOWLEDGMENTS

The authors would like to acknowledge valuable discussions with James M. Rondinelli, Danilo Puggioni, and Shenli Zhang. This research was conducted as part of the Quantum Materials for Energy Efficient Neuromorphic Computing, an Energy Frontier Research Center funded by the US Department of Energy, Office of Science, Basic Energy Sciences under award DE-SC0019273. This research used computational resources of the University of Chicago’s Research Computing Center and at the National Energy Research Scientific Computing Center (NERSC), a DOE Office of Science User Facility supported by the Office of Science of the US Department of Energy.

DATA AVAILABILITY

Data that support the findings of this study will be available through the Qresp [80] curator.

AUTHOR CONTRIBUTIONS

Both authors designed the research and wrote the manuscript. Y.S. performed all calculations.

COMPETING INTERESTS

The authors declare no competing financial or non-financial interests.

- * gagalli@uchicago.edu
- [1] R. Ramesh and D. G. Schlom, Creating emergent phenomena in oxide superlattices, *Nature Reviews Materials* **4**, 257 (2019).
- [2] N. Sicron, B. Ravel, Y. Yacoby, E. A. Stern, F. Dogan, and J. J. Rehr, Nature of the ferroelectric phase transition in PbTiO_3 , *Phys. Rev. B* **50**, 13168 (1994).
- [3] E. A. Stern, Character of order-disorder and displacive components in barium titanate, *Phys. Rev. Lett.* **93**, 037601 (2004).
- [4] A. I. Khan, K. Chatterjee, B. Wang, S. Drapcho, L. You, C. Serrao, S. R. Bakaul, R. Ramesh, and S. Salahuddin, Negative capacitance in a ferroelectric capacitor, *Nature Materials* **14**, 182 (2014).
- [5] M. E. Lines and A. M. Glass, *Principles and applications of ferroelectrics and related materials* (Oxford university press, 1977).
- [6] J. Íñiguez, P. Zubko, I. Luk'yanchuk, and A. Cano, Ferroelectric negative capacitance, *Nature Reviews Materials* **4**, 243 (2019).
- [7] I. B. Bersuker, Pseudo-Jahn–Teller effect—a two-state paradigm in formation, deformation, and transformation of molecular systems and solids, *Chemical Reviews* **113**, 1351 (2013).
- [8] N. A. Hill, Why are there so few magnetic ferroelectrics?, *The Journal of Physical Chemistry B* **104**, 6694 (2000).
- [9] N. A. Spaldin and R. Ramesh, Advances in magnetoelectric multiferroics, *Nature Materials* **18**, 203 (2019).
- [10] E. Bousquet, M. Dawber, N. Stucki, C. Lichtensteiger, P. Hermet, S. Gariglio, J.-M. Triscone, and P. Ghosez, Improper ferroelectricity in perovskite oxide artificial superlattices, *Nature* **452**, 732 (2008).
- [11] C. J. Fennie and K. M. Rabe, Ferroelectric transition in YMnO_3 from first principles, *Phys. Rev. B* **72**, 100103 (2005).
- [12] N. A. Benedek and C. J. Fennie, Hybrid improper ferroelectricity: A mechanism for controllable polarization-magnetization coupling, *Phys. Rev. Lett.* **106**, 107204 (2011).
- [13] N. A. Benedek, J. M. Rondinelli, H. Djani, P. Ghosez, and P. Lightfoot, Understanding ferroelectricity in layered perovskites: new ideas and insights from theory and experiments, *Dalton Transactions* **44**, 10543 (2015).
- [14] J. M. Rondinelli and S. J. May, Deliberate deficiencies: Expanding electronic function through non-stoichiometry, *Matter* **1**, 33 (2019).
- [15] M. T. Anderson, J. T. Vaughey, and K. R. Poeppelmeier, Structural similarities among oxygen-deficient perovskites, *Chemistry of Materials* **5**, 151 (1993).
- [16] V. Chaturvedi, W. M. Postiglione, R. D. Chakraborty, B. Yu, W. Tabiś, S. Hameed, N. Biniskos, A. Jacobson, Z. Zhang, H. Zhou, M. Greven, V. E. Ferry, and C. Leighton, Doping- and Strain-Dependent Electrolyte-Gate-Induced Perovskite to Brownmillerite Transformation in Epitaxial $\text{La}_{1-x}\text{Sr}_x\text{CoO}_{3-\delta}$ Films, *ACS Applied Materials & Interfaces* **13**, 51205 (2021).
- [17] J. Walter, S. Bose, M. Cabero, M. Varela, and C. Leighton, Giant anisotropic magnetoresistance in oxygen-vacancy-ordered epitaxial $\text{La}_{0.5}\text{Sr}_{0.5}\text{CoO}_{3-\delta}$ films, *Phys. Rev. Mater.* **4**, 091401 (2020).
- [18] H. Tian, X.-Y. Kuang, A.-J. Mao, Y. Yang, H. Xiang, C. Xu, S. O. Sayedaghaee, J. Íñiguez, and L. Bellaiche, Novel type of ferroelectricity in brownmillerite structures: A first-principles study, *Phys. Rev. Materials* **2**, 084402 (2018).
- [19] J. Young and J. M. Rondinelli, Crystal structure and electronic properties of bulk and thin film brownmillerite oxides, *Physical Review B* **92**, 174111 (2015).
- [20] T. G. Parsons, H. D'Hondt, J. Hadermann, and M. a. Hayward, Synthesis and Structural Characterization of $\text{La}_{1-x}\text{A}_x\text{MnO}_{2.5}$ (A = Ba, Sr, Ca) Phases: Mapping the Variants of the Brownmillerite Structure, *Chemistry of Materials* **21**, 5527 (2009).
- [21] S. Marik, B. Gonano, F. Veillon, Y. Bréard, D. Pelloquin, V. Hardy, G. Clet, and J. M. Le Breton, Tetrahedral chain ordering and low dimensional magnetic lattice in a new brownmillerite $\text{Sr}_2\text{ScFeO}_5$, *Chem. Commun.* **55**, 10436 (2019).
- [22] J. Young, E. J. Moon, D. Mukherjee, G. Stone, V. Gopalan, N. Alem, S. J. May, and J. M. Rondinelli, Polar oxides without inversion symmetry through vacancy and chemical order, *Journal of the American Chemical Society* **139**, 2833 (2017).
- [23] K. T. Kang, C. J. Roh, J. Lim, T. Min, J. H. Lee, K. Lee, T. Y. Lee, S. Kang, D. Seol, J. Kim, H. Ohta, A. Khare, S. Park, Y. Kim, S. C. Chae, Y. S. Oh, J. Lee, J. Yu, J. S. Lee, and W. S. Choi, A room-temperature ferroelectric ferromagnet in a 1D tetrahedral chain network, *Advanced Materials* **31**, 1808104 (2019).
- [24] R. Arras, C. Paillard, and L. Bellaiche, Effect of an electric field on ferroelectric and piezoelectric properties of brownmillerite $\text{Ca}_2\text{Al}_2\text{O}_5$, *Phys. Rev. B* **107**, 144107 (2023).
- [25] J.-C. Grenier, M. Pouchard, and P. Hagenmuller, Vacancy ordering in oxygen-deficient perovskite-related ferrites, in *Ferrites · Transitions Elements Luminescence* (Springer Berlin Heidelberg, Berlin, Heidelberg, 1981) pp. 1–25.
- [26] L. Yao, S. Inkinen, and S. van Dijken, Direct observation of oxygen vacancy-driven structural and resistive phase transitions in $\text{La}_{2/3}\text{Sr}_{1/3}\text{MnO}_3$, *Nature Communications* **8**, 14544 (2017).
- [27] K. Luo and M. A. Hayward, The synthesis and characterisation of $\text{LaCa}_2\text{Fe}_2\text{GaO}_8$, *Journal of Solid State Chemistry* **198**, 203 (2013).
- [28] S. Zhang and G. Galli, Understanding the metal-to-insulator transition in $\text{La}_{1-x}\text{Sr}_x\text{CoO}_{3-\delta}$ and its applications for neuromorphic computing, *npj Computational Materials* **6** (2020).
- [29] N. Lu, P. Zhang, Q. Zhang, R. Qiao, Q. He, H.-B. Li, Y. Wang, J. Guo, D. Zhang, Z. Duan, Z. Li, M. Wang, S. Yang, M. Yan, E. Arenholz, S. Zhou, W. Yang, L. Gu,

- C.-W. Nan, J. Wu, Y. Tokura, and P. Yu, Electric-field control of tri-state phase transformation with a selective dual-ion switch, *Nature* **546**, 124 (2017).
- [30] A. Shaula, Y. Pivak, J. Waerenborgh, P. Gaczyński, A. Yaremchenko, and V. Kharton, Ionic conductivity of brownmillerite-type calcium ferrite under oxidizing conditions, *Solid State Ionics* **177**, 2923 (2006).
- [31] A. Orera and P. R. Slater, New chemical systems for solid oxide fuel cells, *Chemistry of Materials* **22**, 675 (2010).
- [32] N. Lu, Z. Zhang, Y. Wang, H.-B. Li, S. Qiao, B. Zhao, Q. He, S. Lu, C. Li, Y. Wu, M. Zhu, X. Lyu, X. Chen, Z. Li, M. Wang, J. Zhang, S. C. Tsang, J. Guo, S. Yang, J. Zhang, K. Deng, D. Zhang, J. Ma, J. Ren, Y. Wu, J. Zhu, S. Zhou, Y. Tokura, C.-W. Nan, J. Wu, and P. Yu, Enhanced low-temperature proton conductivity in hydrogen-intercalated brownmillerite oxide, *Nature Energy* **7**, 1208 (2022).
- [33] S. B. Karki and F. Ramezanipour, Pseudocapacitive energy storage and electrocatalytic hydrogen-evolution activity of defect-ordered perovskites $\text{Sr}_x\text{Ca}_{3-x}\text{GaMn}_2\text{O}_8$ ($x = 0$ and 1), *ACS Applied Energy Materials* **3**, 10983 (2020).
- [34] Y. Xie, M. D. Scafetta, R. J. Sichel-Tissot, E. J. Moon, R. C. Devlin, H. Wu, A. L. Krick, and S. J. May, Control of Functional Responses Via Reversible Oxygen Loss in $\text{La}_{1-x}\text{Sr}_x\text{FeO}_{3-\delta}$ Films, *Advanced Materials* **26**, 1434 (2014).
- [35] M. A. Islam, Y. Xie, M. D. Scafetta, S. J. May, and J. E. Spanier, Raman scattering in $\text{La}_{1-x}\text{Sr}_x\text{FeO}_{3-\delta}$ thin films: annealing-induced reduction and phase transformation, *Journal of Physics: Condensed Matter* **27**, 155401 (2015).
- [36] P. Battle, T. Gibb, and P. Lightfoot, The crystal and magnetic structures of $\text{Sr}_2\text{LaFe}_3\text{O}_8$, *Journal of Solid State Chemistry* **84**, 237 (1990).
- [37] S. Y. Smolin, M. D. Scafetta, A. K. Choquette, M. Y. Sfeir, J. B. Baxter, and S. J. May, Static and Dynamic Optical Properties of $\text{La}_{1-x}\text{Sr}_x\text{FeO}_{3-\delta}$: The Effects of A-Site and Oxygen Stoichiometry, *Chemistry of Materials* **28**, 97 (2016).
- [38] H. Guo, Y. Hosaka, F. D. Romero, T. Saito, N. Ichikawa, and Y. Shimakawa, Two Charge Ordering Patterns in the Topochemically Synthesized Layer-Structured Perovskite $\text{LaCa}_2\text{Fe}_3\text{O}_9$ with Unusually High Valence $\text{Fe}^{3.67+}$, *Inorganic Chemistry* **56**, 3695 (2017).
- [39] H. Guo, M. A. Patino, N. Ichikawa, T. Saito, R. Watanabe, M. Goto, M. Yang, D. Kan, and Y. Shimakawa, Oxygen Release and Incorporation Behaviors Influenced by A-Site Cation Order/Disorder in $\text{LaCa}_2\text{Fe}_3\text{O}_9$ with Unusually High Valence $\text{Fe}^{3.67+}$, *Chemistry of Materials* **34**, 345 (2022).
- [40] J. M. Hudspeth, D. J. Goossens, A. J. Studer, R. L. Withers, and L. Norén, The crystal and magnetic structures of $\text{LaCa}_2\text{Fe}_3\text{O}_8$ and $\text{NdCa}_2\text{Fe}_3\text{O}_8$, *Journal of Physics: Condensed Matter* **21**, 124206 (2009).
- [41] X. Martínez de Irujo-Labalde, M. Goto, E. Urones-Garrote, U. Amador, C. Ritter, M. E. Amano Patino, A. Koedtruid, Z. Tan, Y. Shimakawa, and S. García-Martín, Multiferroism induced by spontaneous structural ordering in antiferromagnetic iron perovskites, *Chemistry of Materials* **31**, 5993 (2019).
- [42] A. I. Khan, A. Keshavarzi, and S. Datta, The future of ferroelectric field-effect transistor technology, *Nature Electronics* **3**, 588 (2020).
- [43] J. Zhang, M. Białek, A. Magrez, H. Yu, and J.-P. Ansermet, Antiferromagnetic resonance in TmFeO_3 at high temperatures, *Journal of Magnetism and Magnetic Materials* **523**, 167562 (2021).
- [44] N. Aparnadevi, K. Saravana Kumar, M. Manikandan, D. Paul Joseph, and C. Venkateswaran, Room temperature dual ferroic behaviour of ball mill synthesized NdFeO_3 orthoferrite, *Journal of Applied Physics* **120**, 034101 (2016).
- [45] W. Sławiński, R. Przeniosło, I. Sosnowska, and E. Suard, Spin reorientation and structural changes in NdFeO_3 , *Journal of Physics: Condensed Matter* **17**, 4605 (2005).
- [46] C. Ritter, R. Vilarinho, J. A. Moreira, M. Mihalik, M. Mihalik, and S. Savvin, The magnetic structure of DyFeO_3 revisited: Fe spin reorientation and Dy incommensurate magnetic order, *Journal of Physics: Condensed Matter* **34**, 265801 (2022).
- [47] C. Ritter, M. Ceretti, and W. Paulus, Determination of the magnetic structures in orthoferrite CeFeO_3 by neutron powder diffraction: first order spin reorientation and appearance of an ordered Ce-moment, *Journal of Physics: Condensed Matter* **33**, 215802 (2021).
- [48] P. Prakash, V. Sathe, C. L. Prajapat, A. K. Nigam, P. S. R. Krishna, and A. Das, Spin phonon coupling in mn doped HoFeO_3 compounds exhibiting spin reorientation behaviour, *Journal of Physics: Condensed Matter* **32**, 095801 (2019).
- [49] S. Cao, H. Zhao, B. Kang, J. Zhang, and W. Ren, Temperature induced Spin Switching in SmFeO_3 Single Crystal, *Scientific Reports* **4**, 5960 (2014).
- [50] E. Bertaut, J. Chappert, J. Mareschal, J. Rebouillat, and J. Sivardière, Structures magnetiques de TbFeO_3 , *Solid State Communications* **5**, 293 (1967).
- [51] J. Goodenough, Magnetism and the chemical bond (1963).
- [52] J. Kanamori, Superexchange interaction and symmetry properties of electron orbitals, *Journal of Physics and Chemistry of Solids* **10**, 87 (1959).
- [53] P. W. Anderson, New approach to the theory of superexchange interactions, *Phys. Rev.* **115**, 2 (1959).
- [54] Y. Shin and J. M. Rondinelli, Pressure effects on magnetism in $\text{Ca}_2\text{Mn}_2\text{O}_5$ -type ferrites and manganites, *Physical Review B* **102**, 1 (2020).
- [55] Y. Shin and J. M. Rondinelli, Magnetic structure of oxygen-deficient perovskite nickelates with ordered vacancies, *Phys. Rev. Res.* **4**, L022069 (2022).
- [56] N. A. Spaldin, A beginner's guide to the modern theory of polarization, *Journal of Solid State Chemistry* **195**, 2 (2012).
- [57] R. Resta and D. Vanderbilt, Theory of polarization: A modern approach, in *Physics of Ferroelectrics: A Modern Perspective* (Springer Berlin Heidelberg, Berlin, Heidelberg, 2007).
- [58] S. F. Yuk, K. C. Pitike, S. M. Nakhmanson, M. Eisenbach, Y. W. Li, and V. R. Cooper, Towards an accurate description of perovskite ferroelectrics: exchange and correlation effects, *Scientific Reports* **7**, 43482 (2017).
- [59] D. Waroquiers, X. Gonze, G.-M. Rignanese, C. Welker-Nieuwoudt, F. Rosowski, M. Göbel, S. Schenk, P. Degelmann, R. André, R. Glaum, and G. Hautier, Statistical Analysis of Coordination Environments in Oxides, *Chemistry of Materials* **29**, 8346 (2017).
- [60] R. Mishra, Y.-M. Kim, J. Salafranca, S. K. Kim, S. H. Chang, A. Bhattacharya, D. D. Fong, S. J. Pennycook, S. T. Pantelides, and A. Y. Borisevich, Oxygen-vacancy-

- induced polar behavior in $(\text{LaFeO}_3)_2/(\text{SrFeO}_3)$ superlattices, *Nano Letters* **14**, 2694 (2014).
- [61] N. A. Benedek, Origin of ferroelectricity in a family of polar oxides: The Dion—Jacobson phases, *Inorganic Chemistry* **53**, 3769 (2014).
- [62] X. Z. Lu and J. M. Rondinelli, Epitaxial-strain-induced polar-to-nonpolar transitions in layered oxides, *Nature Materials* **15**, 951 (2016).
- [63] Q. Zhang, A. Solanki, K. Parida, D. Giovanni, M. Li, T. L. C. Jansen, M. S. Pshenichnikov, and T. C. Sum, Tunable ferroelectricity in Ruddlesden–Popper halide perovskites, *ACS Applied Materials & Interfaces* **11**, 13523 (2019).
- [64] C. Becher, L. Maurel, U. Aschauer, M. Lilienblum, C. Magén, D. Meier, E. Langenberg, M. Trassin, J. Blasco, I. P. Krug, P. A. Algarabel, N. A. Spaldin, J. A. Pardo, and M. Fiebig, Strain-induced coupling of electrical polarization and structural defects in SrMnO_3 films, *Nature Nanotechnology* **10**, 661 (2015).
- [65] H. Li, Y. Yang, S. Deng, L. Zhang, S. Cheng, E.-J. Guo, T. Zhu, H. Wang, J. Wang, M. Wu, P. Gao, H. Xiang, X. Xing, and J. Chen, Role of oxygen vacancies in colossal polarization in $\text{SmFeO}_{3-\delta}$ thin films, *Science Advances* **8**, eabm8550 (2022).
- [66] V. Kahlenberg, R. X. Fischer, and C. S. Shaw, Rietveld analysis of dicalcium aluminate ($\text{Ca}_2\text{Al}_2\text{O}_5$) – a new high pressure phase with the brownmillerite-type structure, *American Mineralogist* **85**, 1061 (2000).
- [67] R. Von Schenck and H. Müller-Buschbaum, Über ein neues Erdalkalimetall-Oxoindat: $\text{Sr}_2\text{In}_2\text{O}_5$, *Zeitschrift für anorganische und allgemeine Chemie* **395**, 280 (1973).
- [68] J. P. Perdew, K. Burke, and M. Ernzerhof, Generalized gradient approximation made simple, *Phys. Rev. Lett.* **77**, 3865 (1996).
- [69] P. Giannozzi, S. Baroni, N. Bonini, M. Calandra, R. Car, C. Cavazzoni, D. Ceresoli, G. L. Chiarotti, M. Cococcioni, I. Dabo, A. D. Corso, S. de Gironcoli, S. Fabris, G. Fratesi, R. Gebauer, U. Gerstmann, C. Gougoussis, A. Kokalj, M. Lazzeri, L. Martin-Samos, N. Marzari, F. Mauri, R. Mazzarello, S. Paolini, A. Pasquarello, L. Paulatto, C. Sbraccia, S. Scandolo, G. Sclauzero, A. P. Seitsonen, A. Smogunov, P. Umari, and R. M. Wentzcovitch, QUANTUM ESPRESSO: a modular and open-source software project for quantum simulations of materials, *Journal of Physics: Condensed Matter* **21**, 395502 (2009).
- [70] P. Giannozzi, O. Andreussi, T. Brumme, O. Bunau, M. B. Nardelli, M. Calandra, R. Car, C. Cavazzoni, D. Ceresoli, M. Cococcioni, N. Colonna, I. Carnimeo, A. D. Corso, S. de Gironcoli, P. Delugas, R. A. DiStasio, A. Ferretti, A. Floris, G. Fratesi, G. Fugallo, R. Gebauer, U. Gerstmann, F. Giustino, T. Gorni, J. Jia, M. Kawamura, H.-Y. Ko, A. Kokalj, E. Küçükbenli, M. Lazzeri, M. Marsili, N. Marzari, F. Mauri, N. L. Nguyen, H.-V. Nguyen, A. O. de-la Roza, L. Paulatto, S. Poncé, D. Rocca, R. Sabatini, B. Santra, M. Schlipf, A. P. Seitsonen, A. Smogunov, I. Timrov, T. Thonhauser, P. Umari, N. Vast, X. Wu, and S. Baroni, Advanced capabilities for materials modelling with quantum ESPRESSO, *Journal of Physics: Condensed Matter* **29**, 465901 (2017).
- [71] P. Giannozzi, O. Baseggio, P. Bonfà, D. Brunato, R. Car, I. Carnimeo, C. Cavazzoni, S. de Gironcoli, P. Delugas, F. Ferrari Ruffino, A. Ferretti, N. Marzari, I. Timrov, A. Urru, and S. Baroni, Quantum espresso toward the exascale, *The Journal of Chemical Physics* **152**, 154105 (2020).
- [72] M. Cococcioni and S. de Gironcoli, Linear response approach to the calculation of the effective interaction parameters in the LDA+U method, *Phys. Rev. B* **71**, 035105 (2005).
- [73] V. R. Galakhov, E. Z. Kurmaev, K. Kuepper, M. Neumann, J. A. McLeod, A. Moewes, I. A. Leonidov, and V. L. Kozhevnikov, Valence band structure and x-ray spectra of oxygen-deficient ferrites srfeox, *The Journal of Physical Chemistry C* **114**, 5154 (2010).
- [74] A. Dal Corso, Pseudopotentials periodic table: From H to Pu, *Computational Materials Science* **95**, 337 (2014).
- [75] M. Topsakal and R. Wentzcovitch, Accurate projected augmented wave (PAW) datasets for rare-earth elements (RE=La–Lu), *Computational Materials Science* **95**, 263 (2014).
- [76] R. D. Shannon, Revised effective ionic radii and systematic studies of interatomic distances in halides and chalcogenides, *Acta Crystallographica Section A* **32**, 751 (1976).
- [77] N. Wagner, D. Puggioni, and J. M. Rondinelli, Learning from correlations based on local structure: Rare-earth nickelates revisited, *Journal of Chemical Information and Modeling* **58**, 2491 (2018).
- [78] H. Guo, Z. W. Li, L. Zhao, Z. Hu, C. F. Chang, C.-Y. Kuo, W. Schmidt, A. Piovano, T. W. Pi, O. Sobolev, D. I. Khomskii, L. H. Tjeng, and A. C. Komarek, Antiferromagnetic correlations in the metallic strongly correlated transition metal oxide LaNiO_3 , *Nature Communications* **9**, 43 (2018).
- [79] K. Momma and F. Izumi, *VESTA3* for three-dimensional visualization of crystal, volumetric and morphology data, *Journal of Applied Crystallography* **44**, 1272 (2011).
- [80] M. Govoni, M. Munakami, A. Tanikanti, J. H. Skone, H. B. Runesha, F. Giberti, J. de Pablo, and G. Galli, Qresp, a tool for curating, discovering and exploring reproducible scientific papers, *Scientific Data* **6**, 190002 (2019).

Supplementary Information for

Tunable ferroelectricity in oxygen-deficient perovskites

Yongjin Shin¹ and Giulia Galli^{1,2,3,*}

¹*Pritzker School of Molecular Engineering, University of Chicago, Chicago, Illinois 60637, United States*

²*Department of Chemistry, University of Chicago, Chicago, Illinois 60637, United States*

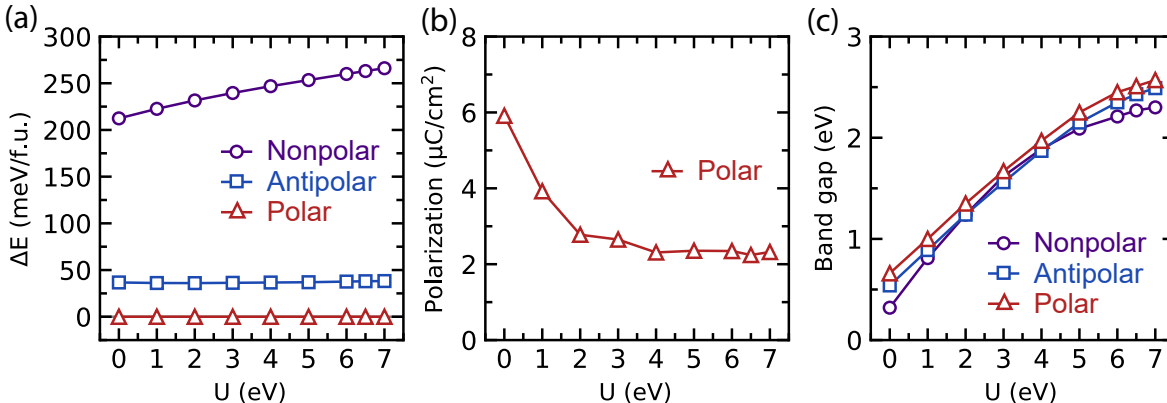
³*Center for Molecular Engineering and Materials Science Division, Argonne National Laboratory, Lemont, Illinois 60439, United States*

*electronic mail: gagalli@uchicago.edu

Contents

Discussion S1. Effect of Hubbard U on computed properties	2
Discussion S2. Effect of spin-orbit coupling on computed properties	3
Discussion S3. Electronic and magnetic properties of the $\text{Nd}_{1/3}\text{Ca}_{2/3}\text{FeO}_{2.67}$ Grenier structure	3
Discussion S4. Effect of cation ordering in $\text{Nd}_{1/3}\text{Ca}_{2/3}\text{FeO}_{2.67}$	5
Discussion S5. Energy differences as a function of cation in $R_{1/3}A_{2/3}\text{FeO}_{2.67}$	6
Discussion S6. Effect of cation size on the structural properties of polar phases of $R_{1/3}A_{2/3}\text{FeO}_{2.67}$	7
Discussion S7. Structural distortions in brownmillerite and Grenier structures	10
References	12

Discussion S1. Effect of Hubbard U on computed properties



Supplementary Figure 1. (a) Energy difference (ΔE) between nonpolar, polar and antipolar phases of $\text{Nd}_{1/3}\text{Ca}_{2/3}\text{FeO}_{2.67}$, as a function of the Hubbard U term used in DFT total energy calculations. (b) Value of the polarization as a function of U . (c) Fundamental band gap as a function of U .

In [Supplementary Figure 1](#), we show how several computed properties of the $\text{Nd}_{1/3}\text{Ca}_{2/3}\text{FeO}_{2.67}$ Grenier structure vary as a function of the value of U used in our DFT calculations. We find that these properties are not sensitive to the U value varying from 0 to 7 eV. Irrespective of the value of U , we find that the ground state of $\text{Nd}_{1/3}\text{Ca}_{2/3}\text{FeO}_{2.67}$ is the polar phase, and that the energy difference between polar and antipolar phases varies within a small energy range, from 36.0 to 38.2 meV/f.u. On the other hand, the energy difference between nonpolar and polar phases increases from 212 to 266 meV/f.u. as U increases.

The spontaneous polarization decreases and converges to a finite value, as U increases, as shown in [Supplementary Figure 1\(b\)](#). The polarization is 5.91 $\mu\text{C}/\text{cm}^2$ at $U = 0$ eV, decreases to 2.7 $\mu\text{C}/\text{cm}^2$ at $U = 2$ eV, and converges to ~ 2.3 $\mu\text{C}/\text{cm}^2$ for $U > 4$ eV. The same convergence to a finite value of the polarization as a function of U is also found in hybrid improper ferroelectric $\text{Ca}_3\text{Ti}_2\text{O}_7$ [1]. Using a large U value leads to an increase in localization of the d -electronic orbitals of the transition metal, which in turns reduces the polarization of ferroelectric structures arising from the second-order Jahn-Teller effect [2]. However, the hybrid improper ferroelectricity and the ferroelectricity found in Grenier phases rely on the rotation of polyhedral units without requiring any off-centering of the transition metal, and thus the value of the spontaneous polarization is insensitive to the choice of the U value.

Finally, in [Supplementary Figure 1\(c\)](#) we show that the fundamental band gap of $\text{Nd}_{1/3}\text{Ca}_{2/3}\text{FeO}_{2.67}$ increases as a function of U for polar, antipolar, and nonpolar phases. $\text{Nd}_{1/3}\text{Ca}_{2/3}\text{FeO}_{2.67}$ remains insulating for all values of the Hubbard U , including 0 eV. Our calculations are consistent with the general effect of U [3, 4] on the computed value of the band gap observed in other materials, where U lowers (increases) the energy of occupied (empty) d bands, thereby increasing the band gap.

Discussion S2. Effect of spin-orbit coupling on computed properties

We investigated the effect of spin-orbit coupling (SOC) on the ferroelectric properties of $\text{Nd}_{1/3}\text{Ca}_{2/3}\text{FeO}_{2.67}$ Grenier structure. In calculations including SOC, we utilized optimized norm-conserving Vanderbilt (ONCV) pseudopotentials, a kinetic energy cutoff of 75 Ry, a k -mesh of $3 \times 8 \times 8$, and a Hubbard U value of 6.5 eV for the structural relaxation. We used the Berry phase method to evaluate the spontaneous polarization. We considered G-AFM order with a collinear spin moment along the z -direction (polar direction) in the $Pmc2_1$ phase, based on experimental observations [5].

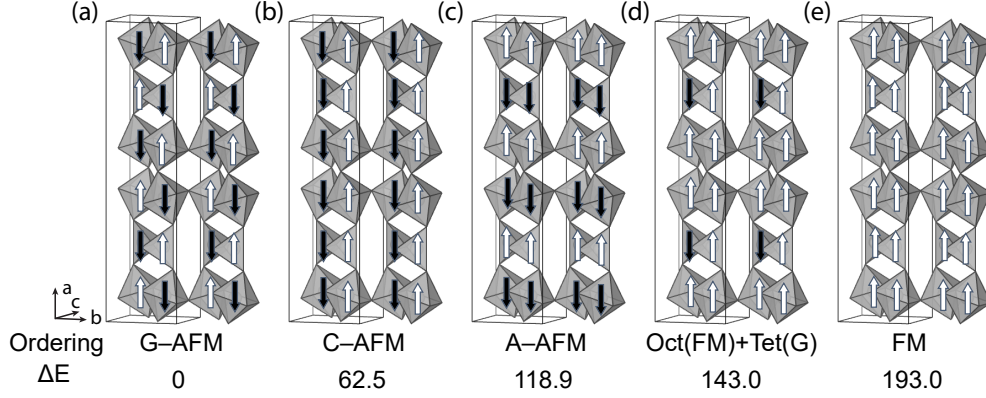
We find that the energy difference between the nonpolar and the polar phase is similar in calculations with and without SOC. Without SOC, the energy difference is 261.6 meV/f.u.; when including SOC the difference slightly reduces to 260.0 meV/f.u. In addition, we find that the spontaneous polarization is relatively insensitive to the inclusion of SOC in our calculations: it increases from $1.71 \mu\text{C}/\text{cm}^2$ to $1.73 \mu\text{C}/\text{cm}^2$ when including SOC. We conclude that overall, the impact of SOC on the ferroelectric properties of the Grenier structure of $\text{Nd}_{1/3}\text{Ca}_{2/3}\text{FeO}_{2.67}$ is not significant.

Discussion S3. Electronic and magnetic properties of the $\text{Nd}_{1/3}\text{Ca}_{2/3}\text{FeO}_{2.67}$ Grenier structure

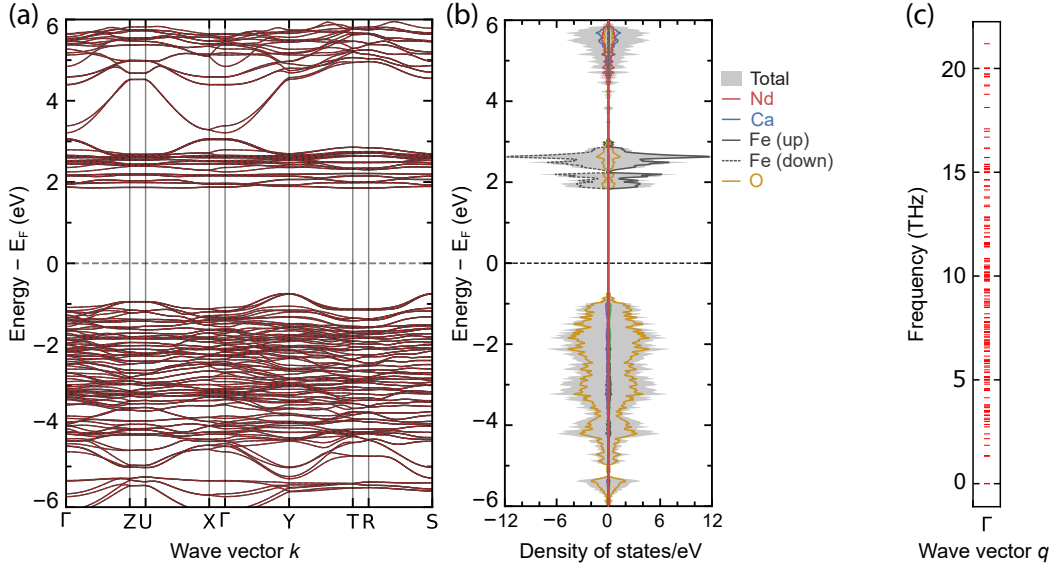
When studying the $\text{Nd}_{1/3}\text{Ca}_{2/3}\text{FeO}_{2.67}$ Grenier structure, we investigated various magnetic ordering commonly observed in perovskite oxides, including ferromagnetic (FM), G-type (G-AFM), A-type (A-AFM), and C-type antiferromagnetic (C-AFM). We also considered the magnetic order found in the $\text{LaCoO}_{2.67}$ Grenier structure [6], where the octahedral layers exhibit FM-coupling within the octahedral layers (with charge ordering and breathing distortion), and AFM-coupling within the tetrahedral layers as shown in [Supplementary Figure 2\(d\)](#). We found that the ground state magnetic order of $\text{Nd}_{1/3}\text{Ca}_{2/3}\text{FeO}_{2.67}$ is G-AFM, which is consistent with the Goodenough-Kanamori-Anderson rule. The Fe^{3+} ions with a high-spin d^5 configuration favors AFM-coupling along the Fe–O–Fe path. The second most stable magnetic order is C-AFM, and its energy difference with respect to G-AFM is 62.5 meV/f.u. Based on this analysis, we considered a G-AFM order for all $R_{1/3}A_{2/3}\text{FeO}_{2.67}$ systems in our study.

Next we computed the ground state properties of the polar Grenier phase of $\text{Nd}_{1/3}\text{Ca}_{2/3}\text{FeO}_{2.67}$ with space group $Pmc2_1$. The electronic band structure and density of states are shown in [Supplementary Figure 3\(a\)](#) and (b). The conduction band is primarily composed of Fe- d orbitals, while the valence band is composed of O- p orbitals. The band gap is 2.51 eV when we apply a U value of 6.5 eV. Due to the antiferromagnetic (AFM) order of the system, the spin-up and spin-down components of Fe-orbitals are symmetric in the band structure and density of states.

To investigate the thermodynamic stability of the polar phase, we performed a frozen phonon calculation using the phonopy package [7]. As shown in [Supplementary Figure 3\(c\)](#), no imaginary phonon frequencies were found at the Γ point, indicating a stable polar phase.



Supplementary Figure 2. Representation of the structure of $\text{Nd}_{1/3}\text{Ca}_{2/3}\text{FeO}_{2.67}$ with different magnetic ordering and their energy differences (meV/f.u.) compared with the ground state magnetic order (G-AFM). Nd, Ca, and O atoms are omitted for clarity. G-AFM corresponds to a checkerboard arrangement of spin moments, while C-AFM involves columnar ordering of spin moments along the a -direction. A-AFM refers to a layered arrangement of spins with the same orientation. In Oct(FM)+Tet(G), ferromagnetic coupling exists within octahedral layers, whereas antiferromagnetic coupling occurs in tetrahedral layers. FM denotes a configuration where all spin moments align in the same direction.



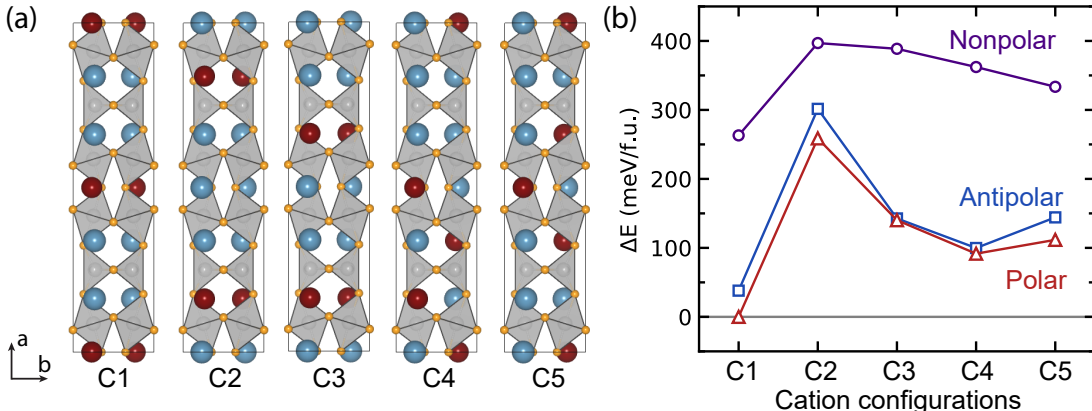
Supplementary Figure 3. Electronic structure of the polar Grenier phase of $\text{Nd}_{1/3}\text{Ca}_{2/3}\text{FeO}_{2.67}$ with $Pmc2_1$ space group and G-type antiferromagnetic order. (a) Band diagram with up- and down-spin components drawn as solid black and dashed darkred lines, respectively. (b) Projected density of states of constituent elements. (c) Phonon frequencies at the Γ point ($6a_p \times 2\sqrt{2}a_p \times 2\sqrt{2}a_p$).

The crystallographic information of the polar $\text{Nd}_{1/3}\text{Ca}_{2/3}\text{FeO}_{2.67}$ phase as obtained from total energy minimizations is provided in [Supplementary Table I](#), where we also give the Born effective charges (BEC) of each Wyckoff positions, obtained from our phonon calculations. Due to the high computational cost of BEC calculations, we used an energy cutoff of 50 Ry and $1 \times 3 \times 3$ k -grid.

Supplementary Table I. Crystallographic data of $\text{Nd}_{1/3}\text{Ca}_{2/3}\text{FeO}_{2.67}$ with $Pmc2_1$ space group, as obtained in our total energy optimization, with $U = 6.5$ eV. Lattice parameters are $a = 11.26434$ Å, $b = 5.57643$ Å, and $c = 5.60952$ Å. Z_{xx}^* , Z_{yy}^* , and Z_{zz}^* are Born effective charge of each ion along a , b , and c -directions, respectively.

Atom	Site	x	y	z	Z_{xx}^*	Z_{yy}^*	Z_{zz}^*
Nd1	2a	0.00000	0.23455	0.81368	3.491	4.281	4.161
Ca1	4c	0.31676	0.22965	0.71415	2.666	2.692	2.569
Fe1	4c	0.82598	0.73780	0.76116	3.638	3.730	3.778
Fe2	2b	0.50000	0.69001	0.70412	3.824	2.525	2.891
O1	4c	0.20388	0.45395	-0.03237	-1.916	-2.513	-2.776
O2	4c	0.86034	-0.03799	0.05114	-2.022	-2.892	-2.853
O3	2b	0.50000	0.37880	0.86289	-1.763	-1.827	-2.749
O4	2a	0.00000	0.65300	0.73409	-2.628	-2.410	-2.058
O5	4c	0.35708	0.83497	0.79854	-3.538	-2.087	-1.657

Discussion S4. Effect of cation ordering in $\text{Nd}_{1/3}\text{Ca}_{2/3}\text{FeO}_{2.67}$



Supplementary Figure 4. (a) Various cation configurations in the $\text{Nd}_{1/3}\text{Ca}_{2/3}\text{FeO}_{2.67}$ Grenier structure (labeled C1 to C5, see text). Red and blue spheres represent Nd and Ca ions, respectively. (b) Total energy differences between polar, antipolar, and nonpolar phases as a function of the configurations shown in (a).

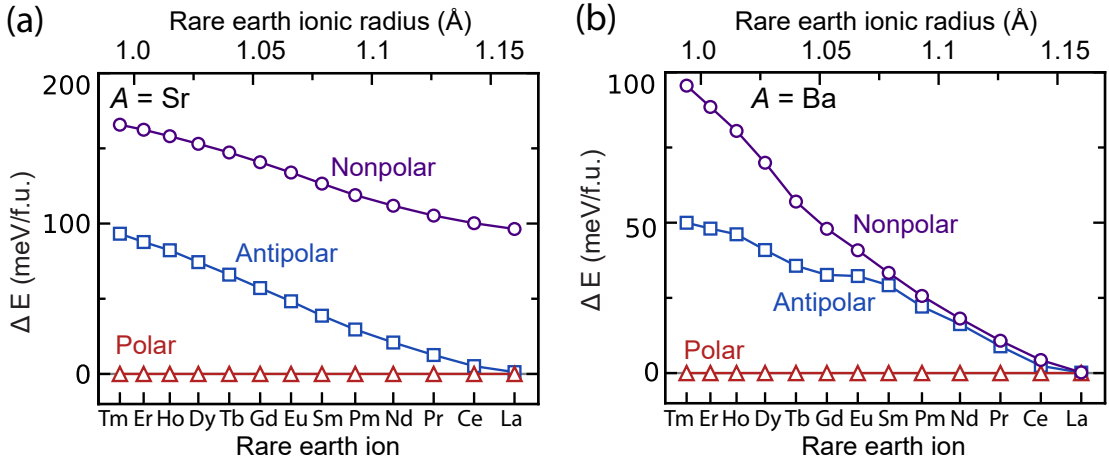
We performed calculations for different geometrical arrangements of Nd (R) and Ca (A) ions in $\text{Nd}_{1/3}\text{Ca}_{2/3}\text{FeO}_{2.67}$, in order to examine the impact of cation ordering in the Grenier structure. The configurations of $\text{Nd}_{1/3}\text{Ca}_{2/3}\text{FeO}_{2.67}$ considered in this work are shown in [Supplementary Figure 4\(a\)](#) and labeled as C1 to C5. In C1, the Nd ions occupy the cation sites between the two octahedral layers, and Ca ions occupy the cation sites in neighboring tetrahedral layers. Because the symmetry of these two sites is different, the space groups of nonpolar, antipolar, and polar phases of C1 are $Pmma$, $Pbcm$, and $Pmc2_1$, respectively, and are equivalent to those of a Grenier structure with homogeneous mixing of R - and A -ions. The configurations labeled (C2–5) are constructed to represent cation mixing different from that of C1 and from homogeneously distributed R - and

A-ions. The configurations C2 and C3 have layered ordering of cations such that equivalent type of cations are arranged on the same ab -plane in the unit cell. On the other hand, C4 and C5 are devised to have nonequivalent cations on the same ab -plane.

Supplementary Figure 4(b) shows the energy differences between polar, nonpolar, and antipolar phases for different configurations (C1–5). For all configurations, we find that polar phases are the lowest in energy, followed by the antipolar phases, indicating that in Grenier structures, ferroelectricity can be realized with various cation arrangements. In the main text, we discuss the ferroelectricity of the Grenier structure based on our results for the “C1” configuration, which was found to be the most stable one, in agreement with the experimental observation that the R -ions preferably occupy the sites between two octahedral layers [8]. The stability of the C1 configuration can be rationalized as follows: the presence of oxygen vacancies creates extra room for cations adjacent to the tetrahedral layers, compared to cations within the octahedral layers. As a result, C1, having relatively large A -cations near the tetrahedral layers and small rare earth ions within the octahedral layers, is energetically favoured.

The energy difference between polar and antipolar phases differ, depending on the configuration chosen: it is 38.0 meV/f.u. for C1, as small as 2.54 meV/f.u. for C3, and as large as 42.8 meV/f.u. for C2. The energy difference between antipolar and nonpolar phases is particularly small for C2, with the total energy of the nonpolar phase only 138.2 meV/f.u. higher than that of the polar phase. The other configurations exhibit energy differences between nonpolar and antipolar phases in the range 222 – 270 meV/f.u.

Discussion S5. Energy differences as a function of cation in $R_{1/3}A_{2/3}\text{FeO}_{2.67}$



Supplementary Figure 5. Total energy differences between polar, antipolar and nonpolar phases of the Grenier $R_{1/3}A_{2/3}\text{FeO}_{2.67}$ solids, as a function of the rare earth ions. (a) and (b) show results for $A = \text{Sr}$ and $A = \text{Ba}$, respectively.

In Supplementary Figure 5, we show the energy differences between the polar, antipolar, and

nonpolar phases of the Grenier structures of $R_{1/3}A_{2/3}\text{FeO}_{2.67}$ with $A = \text{Sr}$ or Ba . We note that these plots are equivalent to those appearing in ??(b). The energy landscape for $A = \text{Sr}$ is similar to that of $A = \text{Ca}$. The polar phases are more stable than nonpolar and antipolar phases and the energy differences gradually increase as the radii of the rare earth elements decrease. We observe an energy difference of 93.2 meV/f.u. for $R = \text{Pm}$, decreasing to 1.22 meV/f.u. for $R = \text{La}$.

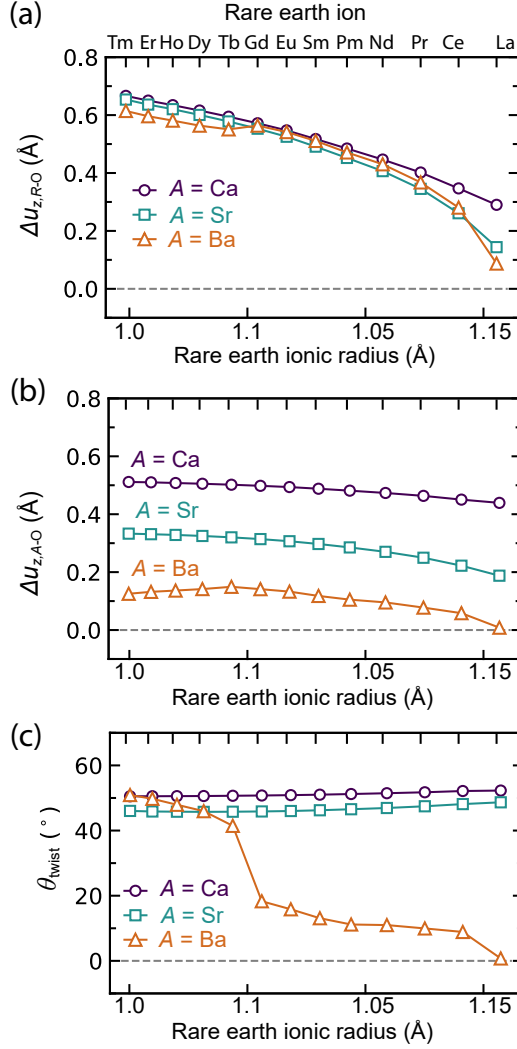
As mentioned in the main text, the presence of a large A cation significantly reduces the energy difference between polar and nonpolar phases, while the effect of the R -ion size on the energy difference is similar for all A -cations. For $A = \text{Ca}$, the energy difference decreases from 320 to 236 meV/f.u. as the atomic radii of the R -ion increases, while for $A = \text{Sr}$, it decreases from 165 to 96 meV/f.u. The main structural difference between the nonpolar and the antipolar phases is the presence of twisted tetrahedral units. The higher energy of the nonpolar phase is associated with an undercoordinated A -cation, where the larger ionic radius of Sr compared to Ca reduces the energy difference between nonpolar and other phases. The size of the R -ion does not play a significant role in the energy difference between nonpolar and antipolar phases because local atomic structures in proximity of the R ion are similar. Indeed, the energy difference between the nonpolar and the antipolar phases is similar for different R -ions.

Also for $A = \text{Ba}$, the polar phase is the ground state for all R -ions; however the energy differences between antipolar and nonpolar phases are significantly smaller compared to the corresponding ones for $A = \text{Ca}$ or Sr . When R is larger than Eu , the nonpolar and antipolar curves in [Supplementary Figure 5\(b\)](#) nearly overlap. For ($R = \text{La}$, $A = \text{Ba}$), all distortion patterns fall within 1 meV/f.u. This small energy difference may be attributed to the small structural differences between the antipolar and nonpolar phases, *e.g.* see the values of θ_{twist} in [Supplementary Figure 6\(c\)](#).

Discussion S6. Effect of cation size on the structural properties of polar phases of $R_{1/3}A_{2/3}\text{FeO}_{2.67}$

In [Supplementary Figure 6](#), we present the structural descriptors that characterize the polar phase of the $R_{1/3}A_{2/3}\text{FeO}_{2.67}$ Grenier structure. These descriptors include the cation-anion displacement along the z -direction in the RO layer ($\Delta u_{z,R-O}$), the displacement in the AO layer ($\Delta u_{z,A-O}$), and the twist angle of the tetrahedral chains (θ_{twist}). The values of these descriptors is zero in the nonpolar phase and the spontaneous polarization varies substantially as a function of these descriptors (??). We found a clear correlations between these descriptors and the size of the R -ion and the A -cations, which we describe in detail below. In this section, we refer to the $R_{1/3}A_{2/3}\text{FeO}_{2.67}$ compounds as (R, A) for brevity.

First, we found that the in-plane atomic displacements, $\Delta u_{z,R-O}$ and $\Delta u_{z,A-O}$, are primarily determined by the size of the R -ion and the A -cations, respectively [[Supplementary Figure 6\(a\)](#) and (b)]. The largest value of $\Delta u_{z,R-O}$ is observed for the smallest cations ($R = \text{Tm}$, $A = \text{Ca}$), reaching 0.67 Å, while the lowest value 0.09 Å is observed for the largest cations ($R = \text{La}$, $A = \text{Ba}$). However, the effect of the A -cation on $\Delta u_{z,R-O}$ indicates that $\Delta u_{z,R-O}$ is mainly determined by the rare

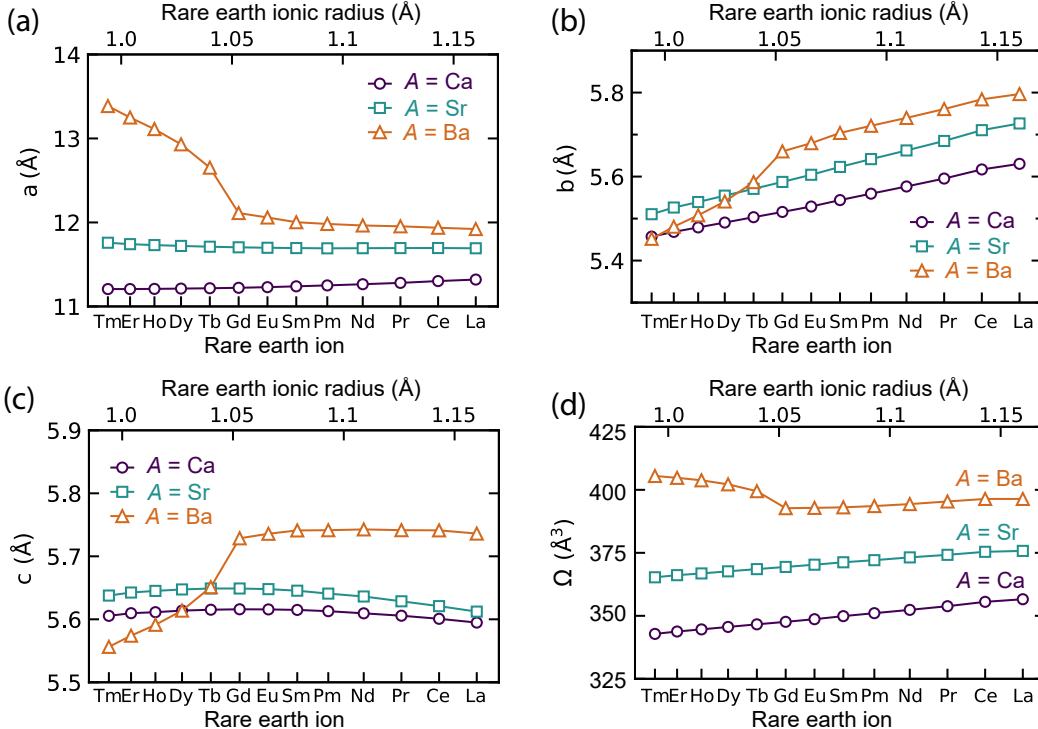


Supplementary Figure 6. Structural descriptors of the polar $R_{1/3}A_{2/3}\text{FeO}_{2.67}$: displacements of (a) R -O and (b) A -O pairs along the polar direction, and (c) twist angle of tetrahedral chains as a function of rare earth elements.

earth species. The curves representing Δu_{A-O} as a function of the A -cations are well-separated in [Supplementary Figure 6\(c\)](#), by approximately 0.2 \AA . In contrast, those as a function of the R -ion differ by approximately 0.1 \AA . Thus the impact of the R -ion on the value of $\Delta u_{z,A-O}$ is smaller than that of the A on Δu_{A-O} .

To illustrate the effect of θ_{twist} , we focus first on the $A = \text{Ca}$ and Sr systems; as for $A = \text{Ba}$ we find a more complex behavior that we discuss separately. Similar to the trend observed for $\Delta u_{z,A-O}$, we find that a smaller cation (Ca) leads to a larger θ_{twist} . This trend can be understood by observing that the twisting of the tetrahedral chain reduces the empty space surrounding A by moving oxygen atoms closer to the A -cations. Hence the presence of smaller A -cation results in a larger twisting motion. Because Ca is smaller than Sr, (R, Ca) solids exhibit larger twist angles than (R, Sr) . Indeed, in brownmillerites smaller A -cations induce larger twist angles in tetrahedral chains

[9–11]. Since the distortion patterns found in Grenier phases are similar to those of brownmillerites, it is reasonable to expect that smaller R -ions and A -cations induce larger distortions also in Grenier phases.



Supplementary Figure 7. Lattice parameters (a , b , and c) and unit cell volume (Ω) of polar phases of $R_{1/3}A_{2/3}FeO_{2.67}$ as a function of rare earth ion R .

Finally, we explain the unique behavior of θ_{twist} for $A = Ba$. While for $A = Ba$, $\Delta u_{z,R-O}$ and $\Delta u_{z,A-O}$ follows the same trend observed for $A = Ca$ and Sr , the trend of θ_{twist} is different. In particular, we find a transition point in going from ($R = Tb$, $A = Ba$) to ($R = Gd$, $A = Ba$), where θ_{twist} drops from 41.5° to 18.3° . When examining the atomic structures of the solids with $A = Ba$, we find that in the presence of smaller R ions, the apical Fe–O bonds of the octahedral units are elongated, resulting in structures where the tetrahedral layers are far apart from the octahedral layers. In such cases, the tetrahedral chains are decoupled from the octahedral units, leading to significantly higher θ_{twist} . These structural properties are consistent with the lattice parameters and unit cell volumes found for the polar phases (Supplementary Figure 7), which clearly points at structural deformations.

It is important to note that such structural deformations occur in the configuration "C1" (see Fig. Supplementary Figure 4). It is reasonable to expect that instead of elongated bonds in the system, cation mixing may be favored, which would reduce the bond elongation. Indeed, the incorporation of Ba into octahedral layers is experimentally observed in $R_{1.2}Ba_{1.2}Ca_{0.6}Fe_3O_8$ ($R = Gd, Tb$) [5].

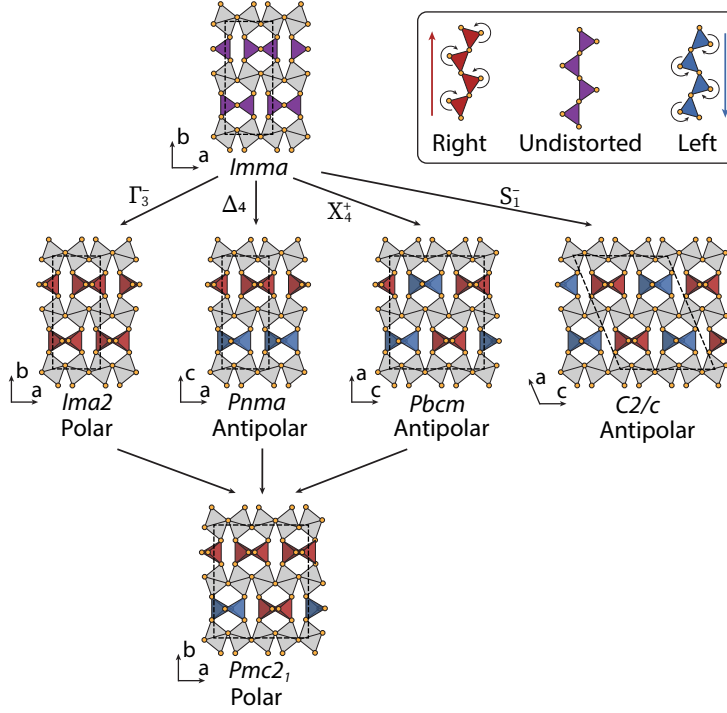
Discussion S7. Structural distortions in brownmillerite and Grenier structures

In [Supplementary Figure 8](#) and [Supplementary Figure 9](#), we present structures originating from distortions of the brownmillerite and Grenier phases, respectively, where we indicate the space group of each structure. It can be challenging to distinguish distortion patterns in these structures, especially if they lead to systems of similar stability. For example, it has been established that the ground state structure of $\text{SrFeO}_{2.5}$ has $Pbcm$ space group, but due to insufficient resolution in several experiments, different space groups had been previously assigned to this system [12]. In general, because both brownmillerite and Grenier structures share similar structural features and show relatively minor variations in oxygen deficiencies, it can be challenging to precisely assign structures in experiments. By identifying the space group associated with each structure, one can help the analysis of samples and the interpretation of their structural motifs, investigate phase transitions in oxygen-deficient phases, and analyze properties related to symmetry breaking.

In the main text, we mainly discussed the twisting of tetrahedral chains where the chains in the same tetrahedral layers exhibit a consistent twisting direction corresponding to space groups $Imma$, $Ima2$, $Pnma$. However, we can obtain additional antipolar phases with larger unit cells where the tetrahedral chains with opposite twisting directions alternate within the same layers. The $Pbcm$ and $C2/c$ space groups both exhibit ‘intra-planar’ alternation of left- and right-handed chains but differ in the stacking of the tetrahedral layers. In the $C2/c$ space group, the same handed chains are aligned along the diagonal direction (a -direction of $C2/c$ in [Supplementary Figure 8](#)). In the $Pbcm$ space group, the same handed chains are aligned in a zigzag pattern along the stacking direction (a -direction of $Pbcm$ in [Supplementary Figure 8](#)). Another type of polar phase, with the $Pmc2_1$ space group, was suggested by Tian *et al.* [11] for $\text{SrCoO}_{2.5}$ brownmillerite, by combining distortions of $Ima2$, $Pnma$, and $Pbcm$. As a result, the structure with $Pmc2_1$ space group has an unequal number of right- and left-handed chains (three right-handed and one left-handed chains in one unit cell) and a polar phase can be stabilized.

We performed DFT calculations for the $A\text{FeO}_{2.5}$ brownmillerite structures and we report our results in [Supplementary Table II](#). The antipolar $Pnma$ structure is the ground state of $\text{CaFeO}_{2.5}$, and the antipolar $C2/c$ structure is the ground state of $\text{SrFeO}_{2.5}$ and $\text{BaFeO}_{2.5}$. We focus on the energy difference between the nonpolar and polar phases compared to the ground state antipolar phases. For $\text{CaFeO}_{2.5}$, where the A -cation ionic radius is small, the polar phase is 22.24 meV/ $\text{CaFeO}_{2.5}$ higher and the nonpolar phase is 330.1 meV/ $\text{CaFeO}_{2.5}$ higher than the antipolar phase. For $\text{SrFeO}_{2.5}$, the energy difference between the antipolar and polar phases is instead very small (less than 1 meV/ $\text{SrFeO}_{2.5}$), but both phases exhibit considerably lower energy compared to that of the nonpolar phase (165 meV/ $\text{SrFeO}_{2.5}$). Finally, for $A = \text{Ba}$, we observe a competitive energy landscape among all nonpolar, polar, and antipolar phases (with energy differences less than 1 meV/ $\text{BaFeO}_{2.5}$).

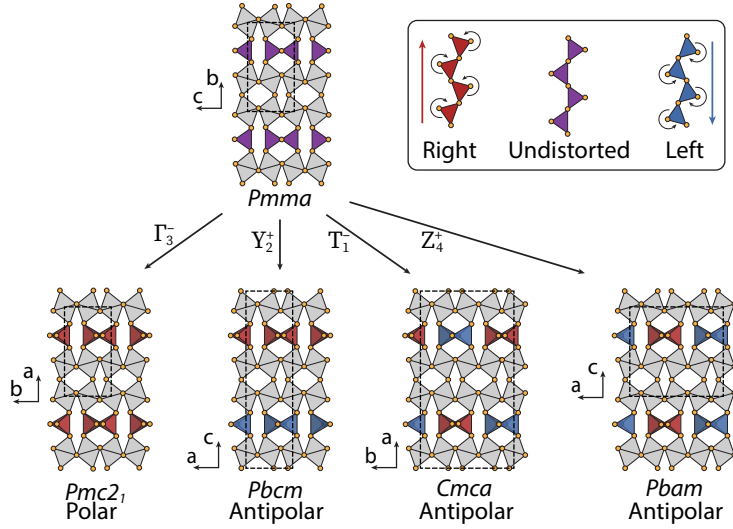
We also conducted a similar analysis for the Grenier structure, as shown in [Supplementary Figure 9](#), utilizing the ISODISTORT [14] and FINDSYM software [15]. By alternating the left-



Supplementary Figure 8. Structural distortions leading to symmetry breaking in the brownmillerite structure. Undistorted tetrahedral chains are represented in purple, and right- and left-handed chains are represented in red and blue, respectively. Unit cells are shown with dashed black lines. The *A*-cations are omitted for clarity. Note that the polar structure with the *Ima2* space group could be equivalently labeled with the *I2bm* [10] and *I2mb* [9, 13] space groups, if different crystallographic axes are chosen. In a similar fashion, *Pbcm* is equivalent to the *Pcmb* space group [9].

and right-handed chains within the same tetrahedral layer, we identified two antipolar phases with *Cmca* and *Pbam* space groups, as illustrated in Supplementary Figure 9. These two space groups differ in the stacking arrangement of tetrahedral layers. In the *Cmca* structure, left- and right-handed chains alternate along the stacking direction (*a*-direction of the *Cmca* phase), whereas in the *Pbam* structure the same type of twisted chains are vertically aligned along the stacking direction (*a*-direction in *Pbam* phase).

We compared the stability of each phase in the case of $\text{Nd}_{1/3}\text{Ca}_{2/3}\text{FeO}_{2.67}$ using DFT calculations and found that the energies of these phases are considerably higher than that of the *Pmc2*₁ phase. Specifically, the *Pbcm* space group structure is 38 meV/f.u. higher than that with the space group *Pmc2*₁, while *Cmca* and *Pbam* structures are 79 and 77 meV/f.u. higher than the polar one, respectively. Therefore, in the main text, we mainly discuss the distortion patterns of the high-symmetry *Pmma* (nonpolar) structure, and the ground state polar (*Pmc2*₁), and the most stable antipolar (*Pbcm*) phases.



Supplementary Figure 9. Structural distortions leading to symmetry breaking in the Grenier structure. Undistorted tetrahedral chains are represented in purple, and right- and left-handed chains are represented in red and blue, respectively. Unit cells are shown with dashed black lines. The R - and A -cations are omitted for clarity. Note that the polar structure with the $Pmc2_1$ space group could be equivalently labeled with the $P2_1ma$ space group, if different crystallographic axes are chosen. In a similar fashion, $Pbcm$ is equivalent to the $Pbma$ space group [13].

Supplementary Table II. Energy differences (ΔE , meV/f.u.) between between polar, nonpolar and antipolar phases relative to their respective ground state (with energy 0) for $AFeO_{2.5}$ brownmillerite structure ($A = Ca, Sr, Ba$) and the Grenier structure of $Nd_{1/3}Ca_{2/3}FeO_{2.67}$.

Space group	CaFeO _{2.5}	SrFeO _{2.5}	BaFeO _{2.5}	Space group	Nd _{1/3} Ca _{2/3} FeO _{2.67}
$Imma$ (non-polar)	330.1	165.0	0.82	$Pmma$ (non-polar)	263.1
$Ima2$ (polar)	22.24	0.98	0.79	$Pmc2_1$ (polar)	0
$Pnma$ (anti-polar)	0	2.32	0.91	$Pbcm$ (anti-polar)	38.01
$Pbcm$ (anti-polar)	26.40	0.17	0.65	$Cmca$ (anti-polar)	79.21
$Pmc2_1$ (polar)	12.81	0.83	7.09	$Pbam$ (anti-polar)	76.80
$C2/c$ (anti-polar)	26.33	0	0		

- [1] C. F. Li, S. H. Zheng, H. W. Wang, J. J. Gong, X. Li, Y. Zhang, K. L. Yang, L. Lin, Z. B. Yan, S. Dong, and J.-M. Liu, Structural transitions in hybrid improper ferroelectric $Ca_3Ti_2O_7$ tuned by site-selective isovalent substitutions: A first-principles study, *Phys. Rev. B* **97**, 184105 (2018).
- [2] N. U. Din, T. Jiang, S. Gholam-Mirzaei, M. Chini, and V. Turkowski, Electron-electron correlations and structural, spectral and polarization properties of tetragonal $BaTiO_3$, *Journal of Physics: Condensed Matter* **32**, 475601 (2020).
- [3] M. Cococcioni and S. de Gironcoli, Linear response approach to the calculation of the effective interaction parameters in the LDA + U method, *Phys. Rev. B* **71**, 035105 (2005).

- [4] Y. Shin and J. M. Rondinelli, Pressure effects on magnetism in $\text{Ca}_2\text{Mn}_2\text{O}_5$ -type ferrites and manganites, *Physical Review B* **102**, 1 (2020).
- [5] X. Martínez de Irujo-Labalde, M. Goto, E. Urones-Garrote, U. Amador, C. Ritter, M. E. Amano Patino, A. Koedtrud, Z. Tan, Y. Shimakawa, and S. García-Martín, Multiferroism induced by spontaneous structural ordering in antiferromagnetic iron perovskites, *Chemistry of Materials* **31**, 5993 (2019).
- [6] N. Biškup, J. Salafranca, V. Mehta, M. P. Oxley, Y. Suzuki, S. J. Pennycook, S. T. Pantelides, and M. Varela, Insulating ferromagnetic LaCoO_3 Films: A Phase Induced by Ordering of Oxygen Vacancies, *Physical Review Letters* **112**, 087202 (2014).
- [7] A. Togo, F. Oba, and I. Tanaka, First-principles calculations of the ferroelastic transition between rutile-type and CaCl_2 -type SiO_2 at high pressures, *Phys. Rev. B* **78**, 134106 (2008).
- [8] J. M. Hudspeth, D. J. Goossens, A. J. Studer, R. L. Withers, and L. Norén, The crystal and magnetic structures of $\text{LaCa}_2\text{Fe}_3\text{O}_8$ and $\text{NdCa}_2\text{Fe}_3\text{O}_8$, *Journal of Physics: Condensed Matter* **21**, 124206 (2009).
- [9] T. G. Parsons, H. D'Hondt, J. Hadermann, and M. a. Hayward, Synthesis and Structural Characterization of $\text{La}_{1-x}\text{A}_x\text{MnO}_{2.5}$ ($A = \text{Ba}, \text{Sr}, \text{Ca}$) Phases: Mapping the Variants of the Brownmillerite Structure, *Chemistry of Materials* **21**, 5527 (2009).
- [10] J. Young and J. M. Rondinelli, Crystal structure and electronic properties of bulk and thin film brownmillerite oxides, *Physical Review B* **92**, 174111 (2015).
- [11] H. Tian, X.-Y. Kuang, A.-J. Mao, Y. Yang, H. Xiang, C. Xu, S. O. Sayedaghaee, J. Íñiguez, and L. Bellaiche, Novel type of ferroelectricity in brownmillerite structures: A first-principles study, *Phys. Rev. Materials* **2**, 084402 (2018).
- [12] J. E. Auckett, A. J. Studer, N. Sharma, and C. D. Ling, Floating-zone growth of brownmillerite $\text{Sr}_2\text{Fe}_2\text{O}_5$ and the observation of a chain-ordered superstructure by single-crystal neutron diffraction, *Solid State Ionics* **225**, 432 (2012).
- [13] K. Luo and M. A. Hayward, The synthesis and characterisation of $\text{LaCa}_2\text{Fe}_2\text{GaO}_8$, *Journal of Solid State Chemistry* **198**, 203 (2013).
- [14] B. J. Campbell, H. T. Stokes, D. E. Tanner, and D. M. Hatch, *ISODISPLACE*: a web-based tool for exploring structural distortions, *Journal of Applied Crystallography* **39**, 607 (2006).
- [15] H. T. Stokes and D. M. Hatch, FINDSYM: program for identifying the space-group symmetry of a crystal, *Journal of Applied Crystallography* **38**, 237 (2005), publisher: International Union of Crystallography.